PHONONIC BAND GAPS IN TWO-DIMENSIONAL PERIODIC STRUCTURES WITH INERTIAL AMPLIFICATION MECHANISMS

by
Gizem DİLBER
B.S., Mechanical Engineering, Boğaziçi University, 2010

Submitted to the Institute for Graduate Studies in
Science and Engineering in partial fulfillment of
the requirements for the degree of
Master of Science

Graduate Program in Mechanical Engineering
Boğaziçi University
2012

This thesis is dedicated to my sister, Sinem, and to my brother, Enes.

ACKNOWLEDGEMENTS

First and foremost I would like to thank Assist. Prof. Çetin Yılmaz for supervising this thesis with his great contributions and innovative ideas. This thesis is a part of his Tubitak career project, and the main idea belongs to him. Besides, he was always available, supportive and encouraging. I would like to thank him for being such a great thesis supervisor.

I also acknowledge Prof. Eşref Eşkinat and Assist. Prof. Arda Deniz Yalçınkaya, for their precious times to read this thesis and giving critical comments about it.

I would like to acknowledge my friends Yağmur, and Mehmet for their encouragement and support. Especially, thank you Mehmet, for always motivating me by asking the state of the thesis, and for your great academic advices.

I would like to thank to my husband, Mustafa Ali, for his dedication and support. As a colleague, his helpful ideas, and technical support play role in this accomplishment, and as a husband, his confidence in me was a great motivation and encouragement.

Finally, I would like to thank to my family, for their encouragement and emotional support. They always motivated me.

This work was supported by Bogazici University Research Grant No. 09HA603P and TUBITAK Grant No. 110M663.

ABSTRACT

PHONONIC BAND GAPS IN TWO-DIMENSIONAL PERIODIC STRUCTURES WITH INERTIAL AMPLIFICATION MECHANISMS

In this thesis, a 2D periodic structure equipped with inertial amplification mechanisms is designed. The structure is optimized to obtain a wide and deep phononic band gap in low frequency ranges. The aim is to prevent wave propagation, hence suppress mechanical vibrations. In the literature, there are two common ways to generate band gaps, Bragg scattering and resonance scattering. Alternative to these methods, inertial amplification method is used in this study. Different types of inertial amplification mechanisms are discussed. Then, a 1D distributed parameter model, which is equivalent to the proposed inertial amplification mechanism is used to construct the 2D periodic structure. First two natural frequencies of the 1D model are found analytically. The model is designed to have a band gap between these two natural frequencies. Yet, in order to calculate the frequencies more accurately, and easily optimize the model, Finite Element Analysis is conducted on the model. The 2D periodic structure is composed of two different 1D unit models. These models are optimized so that the 2D structure has a wide and deep band gap at low frequencies. Prototypes of the two 1D unit models and the 2D structure are produced, and frequency responses of them are obtained by experimental modal analysis. The experimental and numerical frequency response results match quite well, which validate that the 2D structure has a wide and deep band gap.

ÖZET

ATALET ARTIRIMI YÖNTEMİYLE FONON BANT ARALIKLARI GÖSTEREN DÜZLEMSEL PERİYODİK YAPILARIN TASARIMI VE ANALİZİ

Bu tezde atalet artırım mekanizmalarıyla oluşturulmuş iki boyutlu periyodik bir yapı tasarlanmıştır. Bu yapının düşük frekanslarda derin ve geniş fonon bant aralığı göstermesi adına eniyileme çalışması yapılmıştır. Dalga iletiminin engellenmesi ve sonuç olarak mekanik titreşimlerin sönümlenmesi amaçlanmıştır. Literatürde bant aralığı elde etmek için genellikle Bragg saçılımı ve rezonans saçılımı yöntemleri kullanılmıştır. Bu çalışmada, bu yöntemlere alternatif olarak atalet artırım yöntemi kullanılmıştır. Farklı atalet artırım mekanizmaları incelenmiştir. Daha sonra, iki boyutlu periyodik yapının oluşturulmasında seçilen atalet artırım mekanizmasına eşdeğer olan tek boyutlu dağıtık parametreli model kullanılmıştır. Tek boyutlu modelin ilk iki doğal frekansı analitik olarak bulunmuştur. Bu model, ilk iki doğal frekansı arasında bant aralığı gösterecek şekilde tasarlanmıştır. Fakat, doğal frekansları daha doğru bir şekilde hesaplamak ve modelin eniyilemesini yapabilmek için, sonlu elemanlar analizi uygulanmıştır. İki boyutlu periyodik yapı, iki farklı tek boyutlu birim modelin birleştirilmesiyle oluşturulmuştur. Bu modellerin, iki boyutlu yapıda, düşük frekanslarda derin ve geniş bant aralığı elde edilecek şekilde eniyilemesi yapılmıştır. Tek boyutlu birim modellerin ve iki boyutlu yapının prototipleri üretilmiştir, ve bu yapıların frekans cevapları deneysel modal analiz ile bulunmuştur. Deneysel ve nümerik frekans cevapları sonuçları tutarlı bulunmuştur, dolayısıyla iki boyutlu yapının geniş ve derin bir bant aralığının olduğu doğrulanmıştır.

TABLE OF CONTENTS

ACKNOWLEDGEMENTS iv
ABSTRACT v
ÖZET vi
LIST OF FIGURES ix
LIST OF TABLES xiii
LIST OF SYMBOLS xiv
LIST OF ACRONYMS/ABBREVIATIONS xvii
1. INTRODUCTION 1
  1.1. Inertial Amplification 3
    1.1.1. Hydraulic Displacement Amplification 3
    1.1.2. Lever Type Displacement Amplification Mechanism 4
    1.1.3. Geared Type Displacement Amplification Mechanism 5
    1.1.4. Screw-Nut Motion Conversion and Inertial Amplification Mechanism 6
    1.1.5. Bridge Type Displacement Amplification Mechanism 6
  1.2. Motivation and Research Objective 7
2. THEORY AND DESIGN 10
  2.1. Band Gap Generation Methods 10
    2.1.1. Bragg Scattering 10
    2.1.2. Resonance Scattering 14
    2.1.3. Inertial Amplification 16
  2.2. The Design Problem 22
    2.2.1. One-Dimensional Distributed Parameter Model 24
  2.3. Finite Element Analysis 29
    2.3.1. Element Mass and Stiffness Matrices 29
    2.3.2. Assembly of Element Matrices 33
    2.3.3. Branched Model 34
    2.3.4. Boundary Conditions 35
    2.3.5. Modal Analysis 37

2.4. Optimization . . . 38
    2.4.1. Band Structure of the 1D Optimized Model . . . 43
    2.4.2. Array of 1D Unit Models . . . 43
    2.4.3. 2D Distributed Parameter Model . . . 44
    2.4.4. Design of Nodes Connecting 1D Units . . . 47
3. NUMERICAL AND EXPERIMENTAL ANALYSIS OF THE 2D MODEL . . . 50
3.1. Finite Element Analysis . . . 50
    3.1.1. Modal Analysis . . . 50
    3.1.2. Frequency Response . . . 54
3.2. Experimental Results . . . 56
    3.2.1. Production . . . 57
    3.2.2. Impact Test . . . 62
    3.2.3. Frequency Response Function Estimation . . . 63
    3.2.4. Shaker Test . . . 64
4. CONCLUSIONS . . . 69
REFERENCES . . . 71

LIST OF FIGURES

Figure 1.1. Band Structure of the Square Honeycomb Lattice. 2

Figure 1.2. Band Structure of the Hexagonal Honeycomb Lattice. 2

Figure 1.3. Hydraulic Displacement Amplification Mechanism. 4

Figure 1.4. Piezoelectric-Hydraulic Type Displacement Amplification Mechanism. 5

Figure 1.5. Lever Type Displacement Amplification Mechanism. 5

Figure 1.6. Geared Type Displacement Amplification Mechanism. 6

Figure 1.7. Screw-Nut Type Inertial Amplification Mechanism. 7

Figure 1.8. Bridge Type Displacement Amplification Mechanism. 8

Figure 1.9. A Compliant Bridge Type Displacement Amplification Mechanism. 8

Figure 1.10. Sketch of the Lumped Parameter Model. 9

Figure 2.1. Bragg Scattering Example 10

Figure 2.2. Unit Cell of Bragg Scattering Case. 11

Figure 2.3. Band Structure of Bragg Scattering Example 13

Figure 2.4. Frequency Response of Bragg Scattering Example 15

Figure 2.5. Sketch of the Resonance Scattering Example. 16

Figure 2.6. Unit Cell of Resonance Scattering Example. 16

Figure 2.7. Band Structure of Resonance Scattering Example 17

Figure 2.8. Frequency Response of Resonance Scattering Example 18

Figure 2.9. 1D Array of Inertial Amplification Mechanisms. 19

Figure 2.10. Band Structure of Lumped Inertial Amplification Mechanisms. . . 20

Figure 2.11. Frequency Response of Lumped Inertial Amplification Mechanisms. 21

Figure 2.12. Depth and Width of a Band Gap. 22

Figure 2.13. Distributed Parameter Model 24

Figure 2.14. First Mode Shape of the Distributed Parameter Model. 25

Figure 2.15. Second Mode Shape of the Distributed Parameter Model. 27

Figure 2.16. Beam Element with Axial and Bending Coordinates. 29

Figure 2.17. Effect of Eccentricity on Displacements. 31

Figure 2.18. Effect of Eccentricity on Forces and Moments. 32

Figure 2.19. Assembly of Elements. 33

Figure 2.20. Matrix Assembly Procedure. 34

Figure 2.21. Sketch of the Branched Model. 35

Figure 2.22. Global Matrix Assembly Procedure. 36

Figure 2.23. Boundary Conditions of the Distributed Parameter Model. 37

Figure 2.24. Row and Column Deletion for Applying Boundary Conditions. . . 37

Figure 2.25. Transmissibility of the Optimized 1D Model. 42

Figure 2.26. Band Structure of the First Optimized 1D Model. 44

Figure 2.27. Transmissibility of array of units. 45

Figure 2.28. Sketch of the 2D Distributed Parameter Model. 46

Figure 2.29. Band Structure of the Optimized Complementary 1D Model. . . . 47

Figure 2.30. Transmissibility of the Optimized Complementary 1D Model. . . . 48

Figure 3.1. Finite Element Mesh of the 2D Model. 51

Figure 3.2. 43rd Mode Shape for the 2D Optimized Model. 52

Figure 3.3. 44th Mode Shape for the 2D Optimized Model. 53

Figure 3.4. Frequency Response of the Optimized 2D Model. 54

Figure 3.5. Effect of Deviations in Dimensions on the Frequency Response of the 2D Model. 55

Figure 3.6. Effect of Damping on the Frequency Response of the 2D Model. . 56

Figure 3.7. Square Unit Cell of the 2D Optimized Model. 57

Figure 3.8. Prototypes Produced by the Two Providers. 58

Figure 3.9. Impact Test. 63

Figure 3.10. Impact Test Setup. 64

Figure 3.11. Transmissibility of the Unit Square. 65

Figure 3.12. Optimized 2D Model Produced by Provider 1. 66

Figure 3.13. Shaker Test Setup. 66

Figure 3.14. Frequency Response of the Produced 2D Model. 67

Figure 3.15. Frequency Response of the Produced 2D Model in Out-of-Plane Direction. 67

Figure 3.16. Frequency Response of the Produced 2D Model with Extra Damping. 68

Figure 3.17. Frequency Response of the Produced 2D Model with Extra Damping in Out-of-Plane Direction. 68

LIST OF TABLES

Table 2.1. Comparison of Analytical and FEA Natural Frequencies. 40

Table 3.1. t_2 Dimensions of the First Optimized Model. 59

Table 3.2. t_2 Dimensions of the Complementary Optimized Model. 60

Table 3.3. t_2 Dimensions of the First Optimized Models in the Square Unit Cell. 61

Table 3.4. t_2 Dimensions of the 1D Complementary Optimized Models in the Square Unit Cell. 62

Table 3.5. Minimum, Maximum, Average and Standard Deviation Values for t_2 Dimensions of the 1D Optimized Models in the Produced 2D Model. 64

LIST OF SYMBOLS

A_1	Cross-sectional area of the larger pipe
A_2	Cross-sectional area of the smaller pipe
a	Wave number
d_i	Distance between center of the i^th section and the symmetry axis of the model
d	Eccentricity
F_i	Axial force on i^th element
$\mathbf{F}_\mathrm{mod}$	Modified force vector
$\mathbf{F}$	Force vector
I	Mass moment of inertia of the flywheel
$\mathbf{K}_\mathrm{e}$	Element stiffness matrix
$\mathbf{K}_\mathrm{mod}$	Modified stiffness matrix
k	Stiffness
$\tilde{\mathbf{K}}$	Mass normalized stiffness matrix
l_1	Larger lever length of the lever type inertial amplification mechanism
l_2	Smaller lever length of the lever type inertial amplification mechanism
l_i	Length of the i^th section
m_1	Small mass in Bragg Scattering periodic structures
m_1'	Mass of the 1^st segment of the large 1D unit
m_2	Large mass in Bragg Scattering periodic structures
m_a	Mass of the local resonator in resonance scattering example
$\mathbf{M}_\mathrm{e}$	Element mass matrix
m_i	Mass of the i^th section
M_i	Moment on i^th element
m_m	Mass of the main mass in resonance scattering example
$\mathbf{M}_\mathrm{mod}$	Modified mass matrix
m_t	Total mass of the unit cell

m_{x}	Lumped parameter model additional mass
$\mathbf{M}$	Mass matrix
m	Mass
$\mathbf{q}$	Modal coordinate
r	Mean radius of screw
$\mathbf{T}$	Transformation matrix
$\mathbf{T}_{\mathrm{d}}$	Transformation matrix relating the displacements of the eccentric segment to the main axis
$\mathbf{T}_{\mathrm{f}}$	Transformation matrix relating the forces and moments of the eccentric segment to the main axis
t_{i}	Thickness of the i^{th} section
T_{max}	Maximum kinetic energy
T	Kinetic energy
TR	Transmissibility
u_1	Input to the displacement amplification mechanism
u_2	Input from the displacement amplification mechanism
u_{h}	Horizontal displacement
u_{v}	Vertical displacement
V_{i}	Axial displacement
V	Potential energy
W_{i}	Lateral displacement
$x_1^{(n)}$	Displacement of m_1 of n^{th} unit cell
$x_2^{(n)}$	Displacement of m_2 of n^{th} unit cell
X	Frequency domain output
x	Lumped parameter model output coordinate
$\mathbf{x}$	Displacement vector of the finite element
Y	Frequency domain input
y	Input displacement
α	Screw helix angle
γ	Wave vector
ω_{p1}	1st resonance frequency of lumped model

ω_{p2}	2nd resonance frequency of lumped model
ω_{z1}	Antiresonance frequency of lumped model
θ_{i}	Angular displacement
θ	Lumped parameter model angular coordinate

LIST OF ACRONYMS/ABBREVIATIONS

1D	One Dimensional
2D	Two Dimensional
3D	Three Dimensional
DOF	Degree of Freedom
FEA	Finite Element Analysis
FEM	Finite Element Method

1. INTRODUCTION

Prevention of electromagnetic, photonic or elastic wave propagation is a contemporary issue in many engineering applications. Producing band gaps in periodic structures is a very common way for achieving this task [1, 2]. Band gap is defined as the range of frequencies where the wave propagation is prevented. There are two types of band gaps in terms of the wave type, propagation of which is prevented. Phononic band gaps are the range of frequencies where the elastic and acoustic waves do not propagate, whereas in photonic band gaps, electromagnetic and optical wave propagation is prevented [1]. Type and frequency range of band gap vary depending on the application [3–5]. In this thesis, vibration suppression is aimed and a 2D periodic structure with a phononic band gap in lower frequencies is designed.

Band gaps in periodic structures are studied by many researchers [6, 7]. Periodic structures are constructed from repetition of identical parts, called unit cells. Amount of vibration attenuation in the band gap of a periodic structure depends on number of unit cells in it. Attenuation increases with the number of unit cells and no vibration is transmitted in the structure with infinite unit cells. In the literature, wave propagation characteristics for different unit cell shapes are investigated [8, 9]. For example in [9], band structures of lattices with different unit cells, such as square honeycomb, hexagonal honeycomb are compared (see Figures 1.1 and 1.2). The effect of lattice shape on width and directionality characteristics of band gap is also investigated [10].

In solid state physics, construction of different types of lattices with various orientations of atoms is a way commonly used to create photonic band gaps. For example, [6] used fcc type crystals to create photonic band gaps, and they observed that the crystal prevents electromagnetic wave propagation irrespective of its direction.

There are mainly two commonly used ways of creating band gaps, Bragg scattering and resonance scattering.

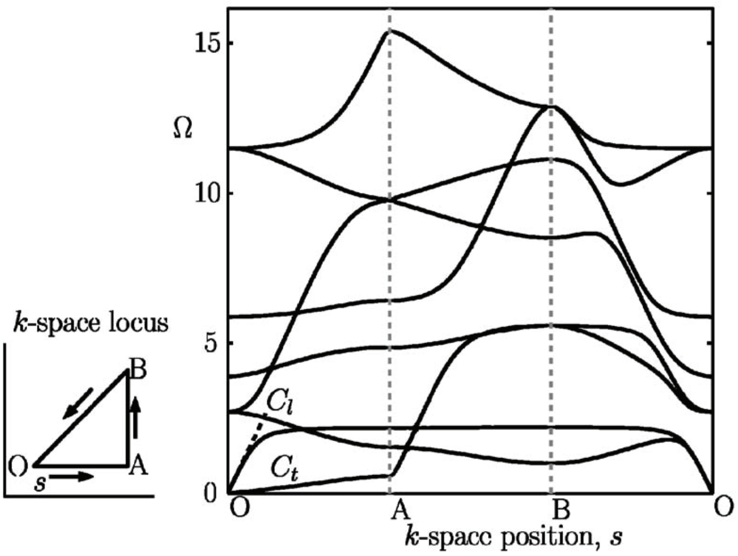

Figure 1.1. Band Structure of the Square Honeycomb Lattice [9].

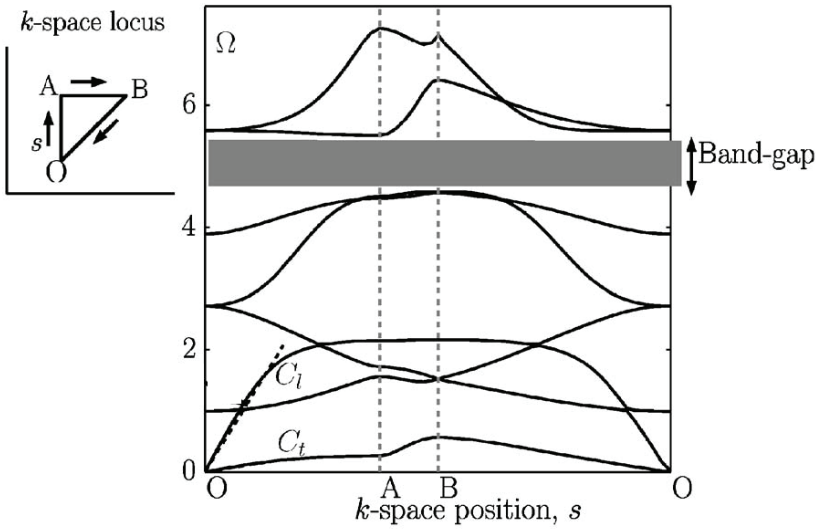

Figure 1.2. Band Structure of the Hexagonal Honeycomb Lattice [9].

Bragg scattering is prevention of wave propagation due to cancellation of transmitted and reflected waves because of the periodic changes in mass and stiffness [11]. A mass spring array in which the masses vary periodically is the most basic example for Bragg scattering case. In the literature, different types of discrete or continuous periodic structures are designed, such as string-mass chains or array of elastic beams connected by couplers [12–14]. These structures have band gaps in some frequency ranges due to Bragg scattering.

Another way to create band gaps is adding local resonators to the system. These resonators extract the energy of the propagating wave when excited around their resonance frequencies. At the natural frequency of the resonator, the whole system has an antiresonance, and the transmissibility goes to zero for no damping case. The band gap starts at this antiresonance, after which the transmissibility plot stays flat and then resonances occur again at higher frequencies [15–17]. In literature, resonance scattering is performed by attaching resonators to the main structure with springs or designing equivalent distributed parameter models [18, 19].

1.1. Inertial Amplification

Alternative to the two common ways of generating band gaps, there is a new band gap generation method based on inertial amplification [20, 21]. When a small mass is attached to the output end of a displacement amplification mechanism, the effective inertia of this small mass can be amplified. Before investigating this band gap generation method, different types of displacement amplification mechanisms are studied. There are several types of displacement amplification mechanisms used to amplify the inertia of a small mass.

1.1.1. Hydraulic Displacement Amplification

Hydraulic displacement amplification mechanisms generally uses the fact that when a fluid flows from a pipe of large cross-section to another of smaller cross-section, its speed increases [22]. A simple sketch of this type of mechanism is given in Figure

1.3.

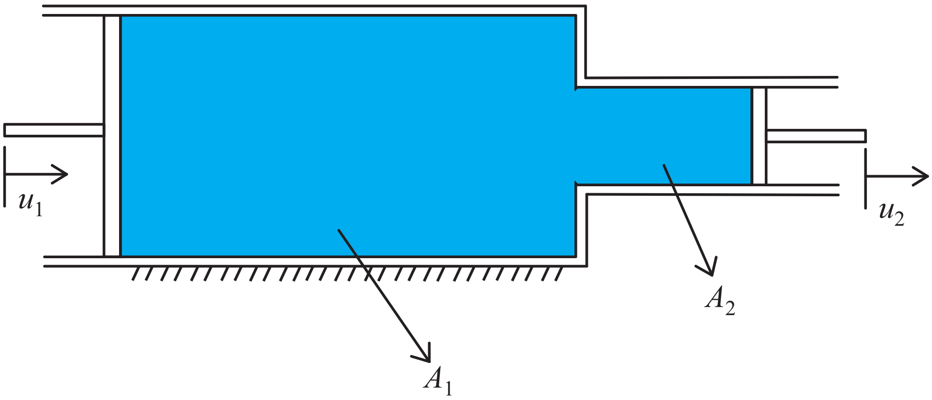

Figure 1.3. Hydraulic Displacement Amplification Mechanism.

As can be seen from Figure 1.3, the displacement is amplified from input to output by an amount of the ratio of the cross sectional areas, A_1/A_2. Hence, the inertia of a small mass attached to the output is amplified via the mechanism. An example of hydraulic type displacement amplification mechanism is given in [23]. This mechanism is used in sensors to amplify the input displacements in order to sense them more accurately.

Another example is given by [22], where a piezoelectric part is used to excite the hydraulic mechanism, which is amplifying the input displacement. A sketch of this mechanism is given in Figure 1.4.

1.1.2. Lever Type Displacement Amplification Mechanism

These types of mechanisms basically amplify the displacement of the input by an amount related to the lever length. An example of a lever type mechanism is given in [24]. As can be seen from the Figure 1.5, the output to input displacement ratio u_2/u_1 is equal to l_1/l_2 [24]. Some displacement amplification mechanisms are constructed by combining the mechanism with a piezoelectric part which helps to increase the amplification ratio. Examples are given in [25], and [26], where the piezoelectric part

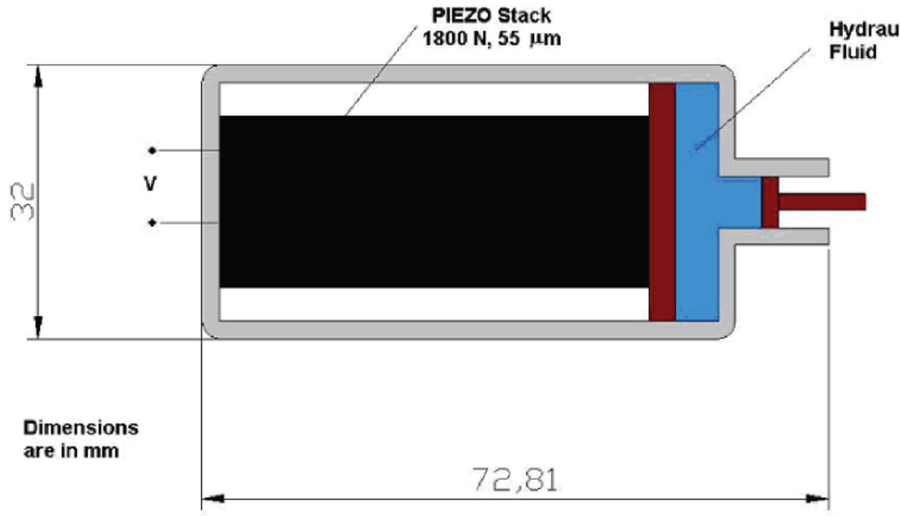

Figure 1.4. Piezoelectric-Hydraulic Type Displacement Amplification Mechanism [22].

is used as input, exciting the levers which amplify the motion applied.

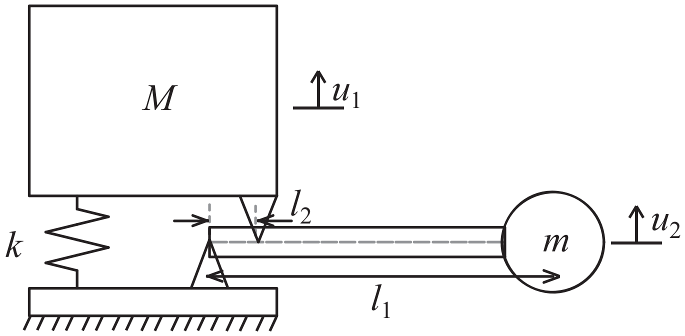

Figure 1.5. Lever Type Displacement Amplification Mechanism [24].

1.1.3. Geared Type Displacement Amplification Mechanism

Geared type mechanisms basically amplify the displacements by using a large gear at the input, which is transmitting the motion to a smaller gear, linked to the output. A mechanism of this type is used by [27], a simple sketch of which is given in Figure 1.6.

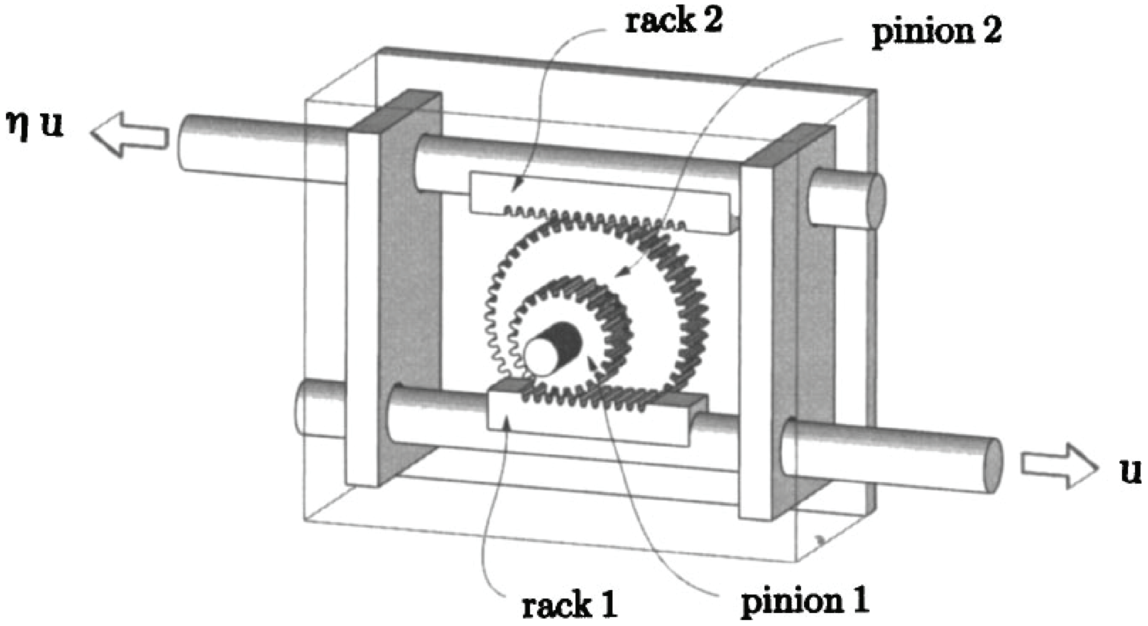

Figure 1.6. Geared Type Displacement Amplification Mechanism. Here, η is the ratio of pinion 2 radius to pinion 1 radius [27] .

1.1.4. Screw-Nut Motion Conversion and Inertial Amplification Mechanism

This type of mechanisms amplify the inertia of a mass by converting its linear motion to rotationary motion via a screw-nut pair. An example given by [28], is illustrated in Figure 1.7. When mass m moves relative to the base, linear motion of the threaded bar 6 causes rotation of the nut/flywheel 4. The effective mass of the flywheel becomes $I/\left(r^2 \tan^2 \alpha\right)$, where I is inertia of the flywheel, r is the mean radius of the screw, and α is the helix angle [28].

1.1.5. Bridge Type Displacement Amplification Mechanism

Bridge type mechanism is another widely used displacement amplification method. These type of mechanisms are generally composed of links and hinges, or equivalent distributed parameter structures. They amplify the input displacement by an amount related to their geometry [29]. A simple sketch of a bridge type mechanism is given

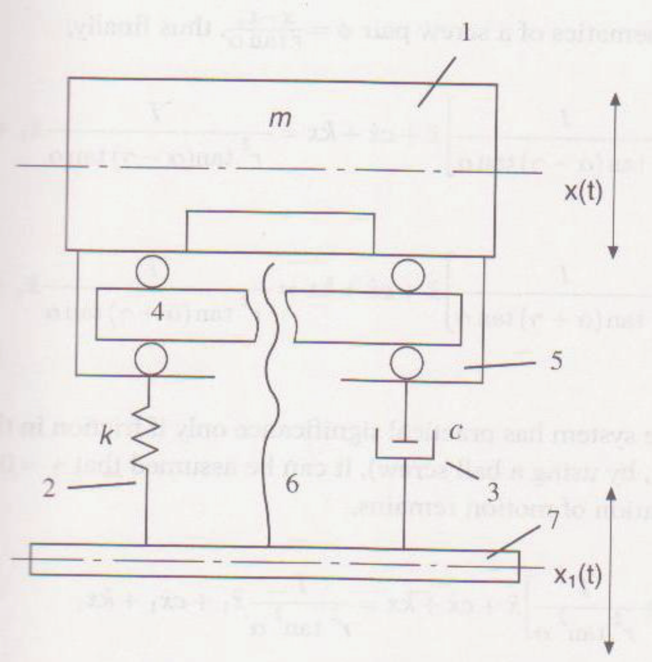

Figure 1.7. Screw-Nut Type Inertial Amplification Mechanism [28].

in Figure 1.8. The input displacement is amplified by an amount related to $\cot\alpha$. An example of a bridge type displacement amplification mechanism is used in [30], and shown in Figure 1.9.

1.2. Motivation and Research Objective

The aim of this project is to design and produce a novel two dimensional periodic structure with a wide and deep phononic band gap in low frequency ranges. Inertial amplification mechanisms in the structure lower the frequency range of the band gap without increasing the overall mass or decreasing the overall stiffness. Motivations behind this research can be summarized as

- Wave propagation through the periodic structure is prevented in the range of frequencies where the band gap occurs. Therefore, the structure can be used as a vibration isolator.

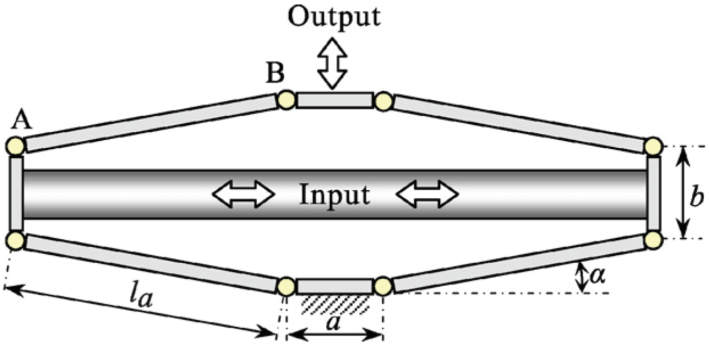

Figure 1.8. Bridge Type Displacement Amplification Mechanism [29].

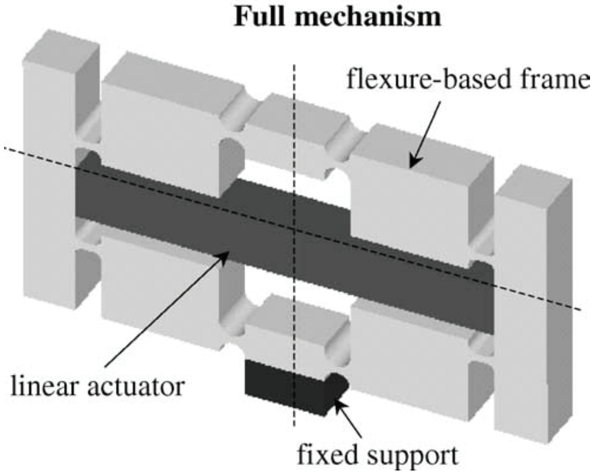

Figure 1.9. A Compliant Bridge Type Displacement Amplification Mechanism [30].

- The structure is a novel one since the inertial amplification mechanisms are used in order to lower the band gap frequency range for the first time.
- Band gaps of smaller structures are generally in higher frequency ranges compared to those of the larger, and massive ones. With inertial amplification mechanisms, a structure in only centimeter scales can have a band gap in a few hundred Hz frequency range where mechanical vibrations usually take place.
- A structure with a wide and deep band gap is effective in suppressing vibrations in a wide range of frequencies.

A 2D periodic structure, suitable for above listed aims, is designed. In this structure, the amplification mechanism is of bridge-type. Firstly, a 1D unit model is designed, which is a distributed parameter model equivalent to the lumped parameter inertial amplification mechanism used in [20]. Then, another 1D unit model having a band gap in the same frequencies is designed, and the 2D model is constructed by assembling these 1D units.

Sketch of the lumped parameter equivalent of the one dimensional unit model is given in Figure 1.10.

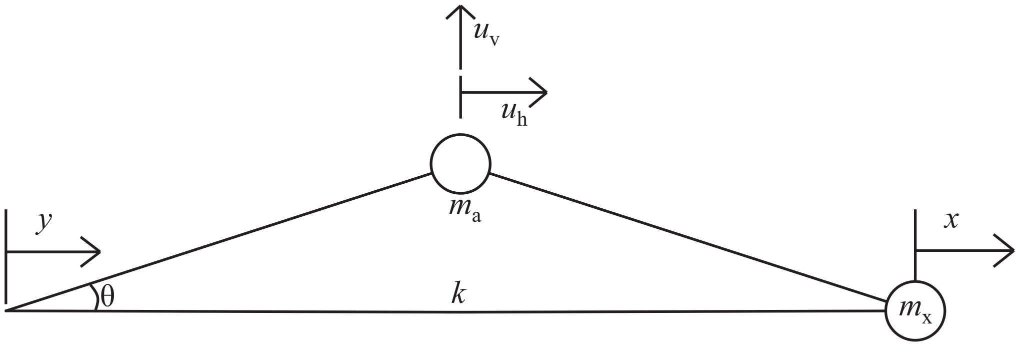

Figure 1.10. Sketch of the Lumped Parameter Model.

2. THEORY AND DESIGN

The aim of this thesis is to design and produce a two dimensional periodic structure with a wide and deep phononic band gap at low frequency ranges.

2.1. Band Gap Generation Methods

Bragg scattering and resonance scattering are two commonly used methods in band gap creation. In this thesis, a new method is utilized. Inertial amplification mechanisms are used in order to obtain deep and wide band gaps in low frequency ranges.

2.1.1. Bragg Scattering

In this method, the structure is formed so that in certain frequency ranges, the interference of the transmitted and reflected waves attenuates the energy of the propagating wave. In some frequency ranges, waves moving in different directions cancel out, and this creates a band gap. A mass-spring system, shown in Figure 2.1, is used to demonstrate a 1D periodic structure with a band gap due to Bragg scattering.

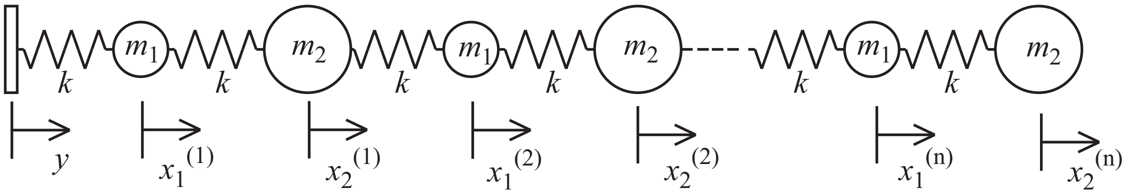

Figure 2.1. Mass Spring Array Used to Show Band Gap due to Bragg Scattering.

There are two ways to obtain the response of the system. First one is by analyzing the unit cell, the band structure can be plotted, and the band gap for the whole system can be obtained by assuming periodic boundary conditions. This method is valid for an infinitely periodic structure. The other one is to plot the transmissibility for a certain number of unit cells. The frequency ranges where the vibration is suppressed can be considered as band gap in the infinitely periodic case. This relation can be seen by comparing the band structure of the infinitely periodic structure and the transmissibility plot of the finite periodic structure. The band structure can be obtained by just analyzing a unit cell, whereas for the transmissibility plot, the whole system of equations must be solved simultaneously. Yet, the advantage of the transmissibility plot is that the individual resonances of the system can be seen directly.

Band structure of the system can be obtained by analyzing the unit cell which is given in Figure 2.2. Here, periodic boundary conditions are assumed.

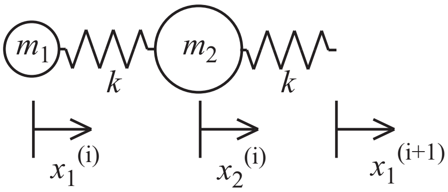

Figure 2.2. Unit Cell of Bragg Scattering Case.

The equations of motion are given in Equation 2.1 and Equation 2.2.

$$m_1\ddot{x_1}^{(i)} + 2kx_1^{(i)} - kx_2^{(i-1)} - kx_2^{(i)} = 0 \tag{2.1}$$

$$m_2\ddot{x_2}^{(i)} + 2kx_2^{(i)} - kx_1^{(i)} - kx_1^{(i+1)} = 0 \tag{2.2}$$

To construct the band structure of the system, Bloch's theorem is used [31].

$$x_{\mathrm{j}}^{(n+m)} = x_{\mathrm{j}}^{(n)} e^{i\gamma \mathbf{T} m} \tag{2.3}$$

In Equation 2.3, displacements of $(n+m)^{\mathrm{th}}$ unit are related to those of n^{th} unit. $\mathbf{T}$ is the transformation matrix relating the orientation of the $(n+m)^{\mathrm{th}}$ unit to that of n^{th} one, and γ is the wave vector, defined as $\gamma = 2\pi a d$, where d is the length of the unit and a is the wave number, defined as $a = 1/\lambda$. The minimum physically possible wavelength is $2d$. Energy of any higher frequency wave is not transmitted through the lattice. Therefore, $a_{max} = 1/2d$ and the limiting value for the wave vector is $\gamma_{max} = \pi$.

Since the system is one dimensional, $\mathbf{T} = 1$. Inserting this expression into Equation 2.1 and Equation 2.2, Equation 2.4 and Equation 2.5 are obtained.

$$m_1 \ddot{x_1}^{(i)} + 2kx_1^{(i)} - kx_2^{(i)}\left(1 + e^{-i\gamma}\right) = 0 \tag{2.4}$$

$$m_2 \ddot{x_2}^{(i)} + 2kx_2^{(i)} - kx_1^{(i)}\left(1 + e^{i\gamma}\right) = 0 \tag{2.5}$$

Equations 2.4 and 2.5 are solved for γ between 0 and π, for two different cases, $m_1/m_{\text{t}} = 0.4$ and $m_1/m_{\text{t}} = 0.1$, where $m_{\text{t}} = m_1 + m_2$. Band structures are given in Figure 2.3. One can see that for the smaller m_1/m_{t} ratio, there is a larger band gap.

For a finite number of unit cells, the frequency response of the mass spring array is obtained by solving the system of coupled equations of motion. Equations of motion for each individual mass are given in Equations 2.6 to 2.11.

$$m_1 \ddot{x_1}^{(1)} + 2kx_1^{(1)} - kx_2^{(1)} = ky \tag{2.6}$$

$$m_2 \ddot{x_2}^{(1)} + 2kx_2^{(1)} - kx_1^{(1)} - kx_1^{(2)} = 0 \tag{2.7}$$

$$m_1 \ddot{x_1}^{(2)} + 2kx_1^{(2)} - kx_2^{(2)} - kx_2^{(1)} = 0 \tag{2.8}$$

$$m_2 \ddot{x_2}^{(2)} + 2kx_2^{(2)} - kx_1^{(2)} - kx_1^{(3)} = 0 \tag{2.9}$$

$$\vdots$$

$$m_1 \ddot{x_1}^{(n)} + 2kx_1^{(n)} - kx_2^{(n)} - kx_2^{(n-1)} = 0 \tag{2.10}$$

$$m_2 \ddot{x_2}^{(n)} + kx_2^{(n)} - kx_1^{(n)} = 0 \tag{2.11}$$

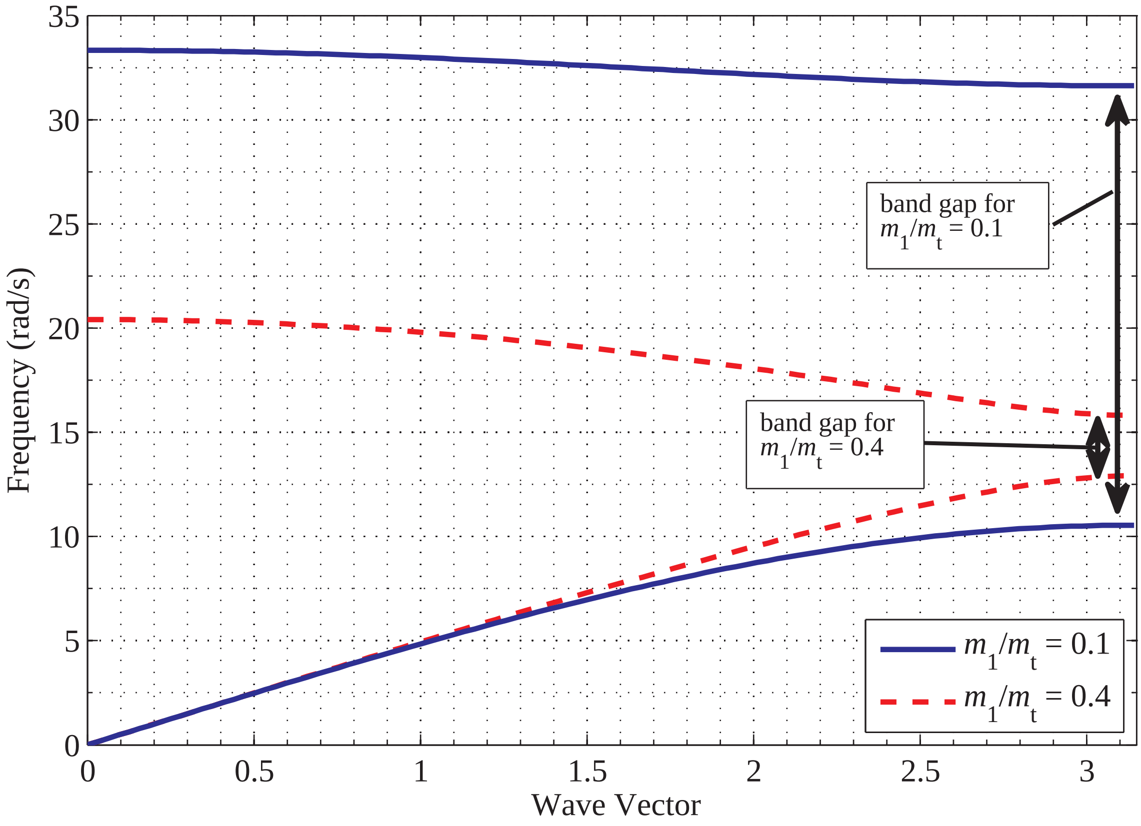

Figure 2.3. Band Structure of Bragg Scattering Example, for Cases $m_1/m_\mathrm{t} = 0.4, m_\mathrm{t} = 0.2, k = 10$ and $m_1/m_\mathrm{t} = 0.1, m_\mathrm{t} = 0.2, k = 10$.

The system of equations (in matrix form) is given in Equation 2.12,

$$\mathbf{M}\ddot{\mathbf{x}} + \mathbf{K}\mathbf{x} = \mathbf{f} \tag{2.12}$$

where

$$\mathbf{M} = \begin{bmatrix} m_1 & 0 & \dots & \dots & 0 \\ 0 & m_2 & & & \vdots \\ \vdots & & m_1 & & \vdots \\ \vdots & & & \ddots & 0 \\ 0 & \dots & \dots & 0 & m_2 \end{bmatrix}, \mathbf{K} = \begin{bmatrix} 2k & -k & 0 & \dots & 0 \\ -k & 2k & -k & & \vdots \\ 0 & -k & 2k & & \vdots \\ \vdots & & & \ddots & -k \\ 0 & \dots & \dots & -k & k \end{bmatrix}, \mathbf{f} = \begin{bmatrix} ky \\ 0 \\ 0 \\ \vdots \\ 0 \end{bmatrix}.$$

For harmonic excitation, Equation 2.12 becomes

$$\left(-\omega^2\mathbf{M}+\mathbf{K}\right)\mathbf{x}=\mathbf{f}. \tag{2.13}$$

The frequency response of the system is given in Equation 2.14.

$$\mathbf{x}=\left(-\omega^2\mathbf{M}+\mathbf{K}\right)^{-1}\mathbf{f}. \tag{2.14}$$

For the mass spring array given in Figure 2.1, with 5 unit cells, frequency response of $m_1/m_\mathrm{t}=0.4$ and $m_1/m_\mathrm{t}=0.1$ cases are obtained by solving Equation 2.14. Frequency responses are plotted in Figure 2.4. In Figure 2.4, the first set of peaks correspond to the larger masses, and the last set of peaks correspond to the smaller ones. As can be seen from the plot, wider band gaps can be obtained by decreasing the mass ratio m_1/m_t. Besides, by comparing Figure 2.4 with Figure 2.3, one can see that the band gap frequencies overlap.

2.1.2. Resonance Scattering

Resonance scattering is obtained by adding local resonators to the main structure. The system has antiresonances at the natural frequencies of the local resonators. Around these frequencies, the wave propagation is prevented. An example of local resonator is a small mass attached to the main system via a spring. Sketch of a system with local resonators attached to each unit cell is given in Figure 2.5.

In order to construct the band structure of the system, the unit cell of the system is analyzed. Sketch of the unit cell is given in Figure 2.6. Equations of motion of the unit cell are given in Equation 2.15 and Equation 2.16.

$$m_\mathrm{m}\ddot{x}_1{}^{(n)}+k_1\left(2x_1^{(n)}-x_1^{(n-1)}-x_1^{(n+1)}\right)+k_2\left(x_1^{(n)}-x_2^{(n)}\right)=0 \tag{2.15}$$

$$m_\mathrm{a}\ddot{x}_2{}^{(n)}+k_2\left(x_2^{(n)}-x_1^{(n)}\right)=0 \tag{2.16}$$

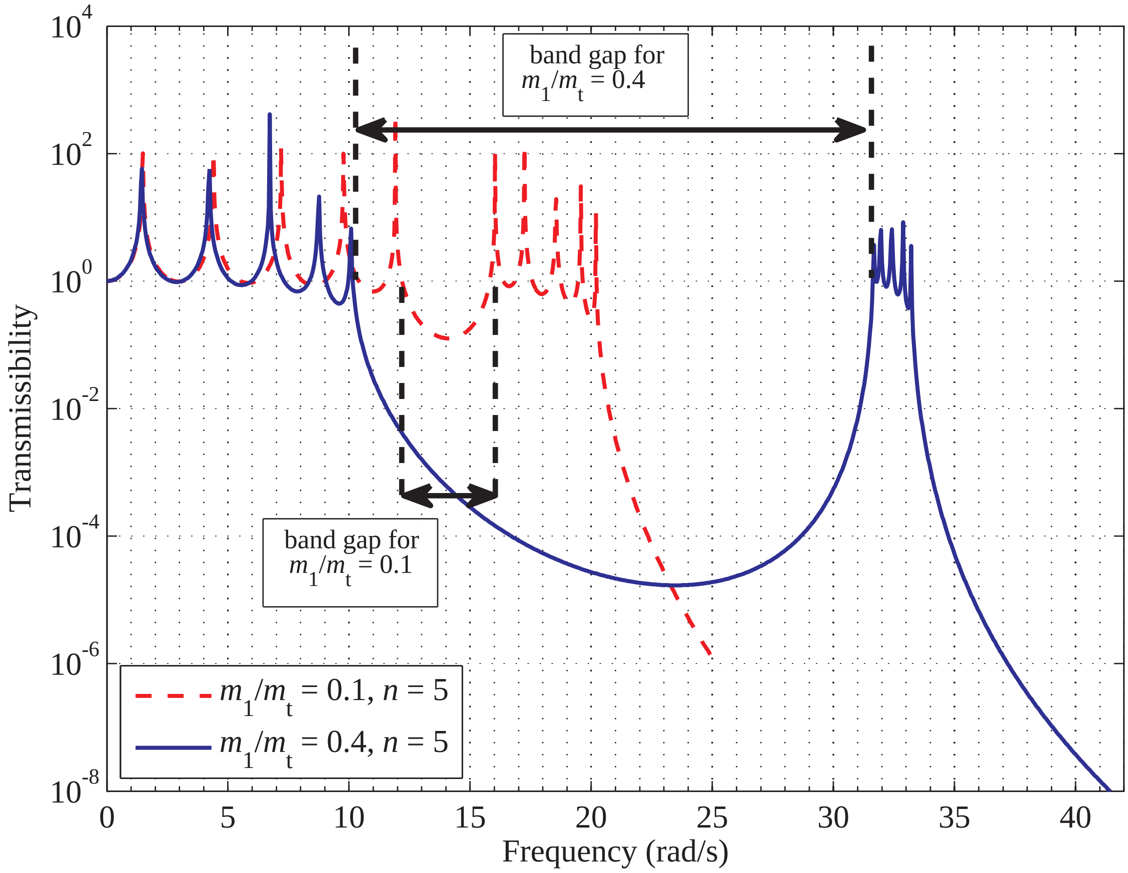

Figure 2.4. Frequency Response of Bragg Scattering Example, for Cases $m_1/m_\text{t} = 0.4, n = 5$ and $m_1/m_\text{t} = 0.1, n = 5$.

Using Bloch's theorem, equations of motion are decoupled from the other unit cells and given in Equation 2.17 and Equation 2.18.

$$m_\text{m}\ddot{x}_1{}^{(n)} + k_1 x_1^{(n)} \left(2 - e^{-i\gamma} - e^{i\gamma}\right) + k_2 \left(x_1^{(n)} - x_2^{(n)}\right) = 0 \tag{2.17}$$

$$m_\text{a}\ddot{x}_2{}^{(n)} + k_2 \left(x_2^{(n)} - x_1^{(n)}\right) = 0 \tag{2.18}$$

For two different cases, $m_\text{a}/m_\text{t} = 0.4, k_2/k_1 = 1$ and $m_\text{a}/m_\text{t} = 0.4, k_2/k_1 = 5$, band structures are plotted, given in Figure 2.7. As can be seen from Figure 2.7, band gap is wider for the larger k_2/k_1 ratio.

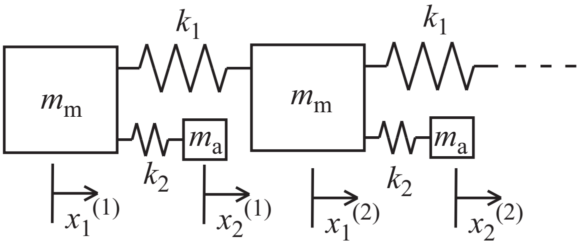

Figure 2.5. Sketch of the Resonance Scattering Example.

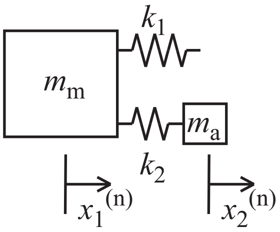

Figure 2.6. Unit Cell of Resonance Scattering Example.

For the system given in Figure 2.5, with 5 unit cells, frequency response of $m_\text{a}/m_\text{t} = 0.4, k_2/k_1 = 1$ and $m_\text{a}/m_\text{t} = 0.4, k_2/k_1 = 5$ cases are obtained by solving the system of coupled equations of motion. Frequency response of the two case are plotted, given in Figure 2.8. By comparing Figure 2.8 with Figure 2.7, one can see that the band gap frequency ranges overlap.

2.1.3. Inertial Amplification

In this method, inertia of a small mass is amplified by displacement amplification mechanisms. The lumped parameter model of the inertial amplification mechanism used in this thesis is composed of two rigid links connected directly from one end with an attached point mass, and connected via a spring from the other end, as shown in Figure 1.10. For small θ values, the displacement of the ends of the spring is amplified through the mechanism, and the displacement of the point mass is greater for smaller θ

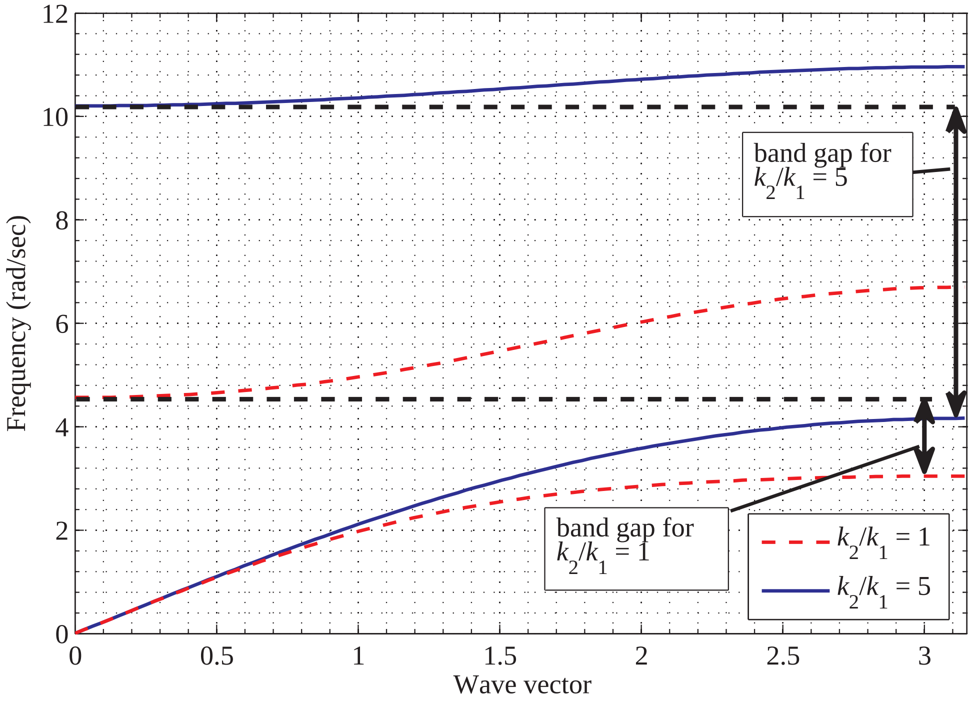

Figure 2.7. Band Structure of Resonance Scattering Example, for Cases $m_\mathrm{a}/(m_\mathrm{m}+m_\mathrm{a}) = 0.4, k_2/k_1 = 1$ and $m_\mathrm{a}/(m_\mathrm{m}+m_\mathrm{a}) = 0.4, k_2/k_1 = 5$.

values. The relation between the end displacements and the displacement of the point mass is given in Equation 2.19 and Equation 2.20.

$$u_\mathrm{h} = \frac{x+y}{2} \tag{2.19}$$

$$u_\mathrm{v} = \frac{y-x}{2}\cot\theta \tag{2.20}$$

The potential and the kinetic energy of the lumped parameter model are given

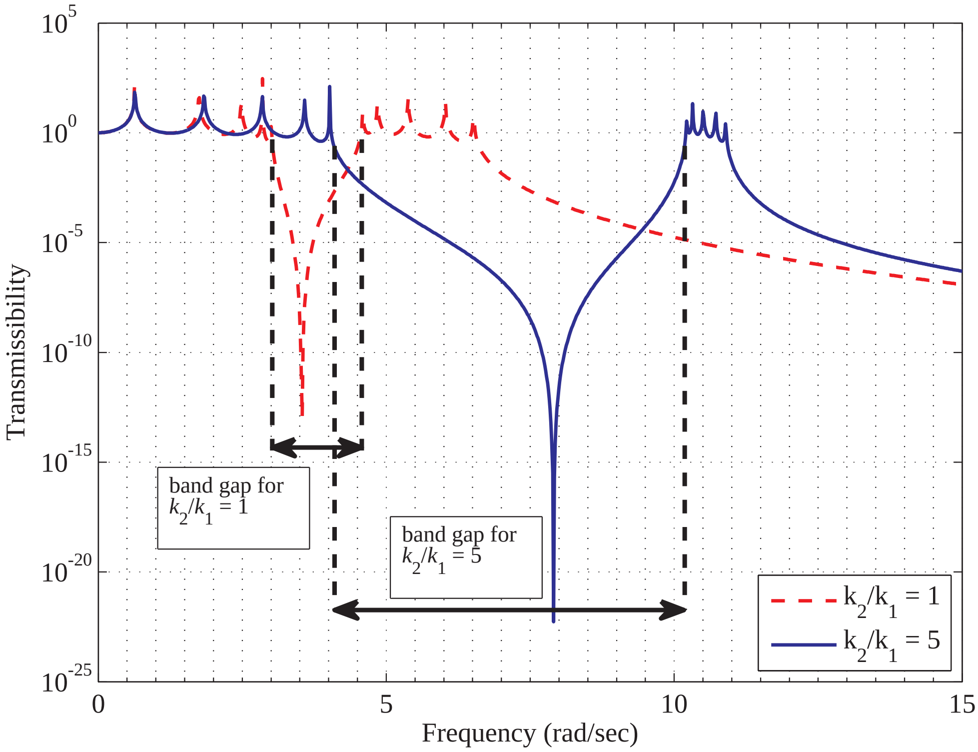

Figure 2.8. Frequency Response of Resonance Scattering Example, for Cases $m_\mathrm{a}/(m_\mathrm{m}+m_\mathrm{a}) = 0.4, k_2/k_1 = 1$ and $m_\mathrm{a}/(m_\mathrm{m}+m_\mathrm{a}) = 0.4, k_2/k_1 = 5$.

in Equation 2.21 and Equation 2.22, respectively.

$$V = \frac{1}{2}k\left(x-y\right)^2 \tag{2.21}$$

$$T = \frac{1}{2}m_\mathrm{a}\left(\left(\frac{\dot{x}+\dot{y}}{2}\right)^2 + \left(\frac{\dot{x}-\dot{y}}{2}\cot\theta\right)^2\right) + \frac{1}{2}m_\mathrm{x}\dot{x}^2 \tag{2.22}$$

In order to find the resonance and antiresonance frequency of the lumped parameter model, equation of motion is written using Lagrange method. The Lagrangian of the model is $L = T - V$, and Lagrange's equation for x coordinate is given in Equation 2.23.

$$\frac{d}{dt}\left(\frac{\partial L}{\partial \dot{x}}\right) - \frac{\partial L}{\partial x} = \frac{d}{dt}\left(\frac{\partial T}{\partial \dot{x}}\right) + \frac{\partial V}{\partial x} = 0 \tag{2.23}$$

Equation of motion is found by inserting kinetic and potential energy expressions into Equation 2.23. The equation of motion is given in Equation 2.24.

$$\left(m_{\mathrm{a}}\left(\cot^2\theta+1\right)+4m_{\mathrm{x}}\right)\ddot{x}+4kx=m_{\mathrm{a}}\ddot{y}\left(\cot^2\theta-1\right)+4ky \tag{2.24}$$

By considering y as input and x as output, the resonance and antiresonance frequencies are found and given in Equation 2.25, and Equation 2.26, respectively.

$$\omega_{\mathrm{p1}}=\sqrt{\frac{4k}{m_{\mathrm{a}}\left(\cot^2\theta+1\right)+4m_{\mathrm{x}}}} \tag{2.25}$$

$$\omega_{\mathrm{z1}}=\sqrt{\frac{4k}{m_{\mathrm{a}}\left(\cot^2\theta-1\right)}} \tag{2.26}$$

1D array of inertial amplification mechanisms is analyzed. The array is given in Figure 2.9. Equation of motion for a unit cell is given in Equation 2.27. In order to decouple the equation from the neighboring unit cell, $x^{(i-1)}=x^{(i)}e^{-i\gamma}$ is inserted into Equation 2.27 and Equation 2.28 is obtained.

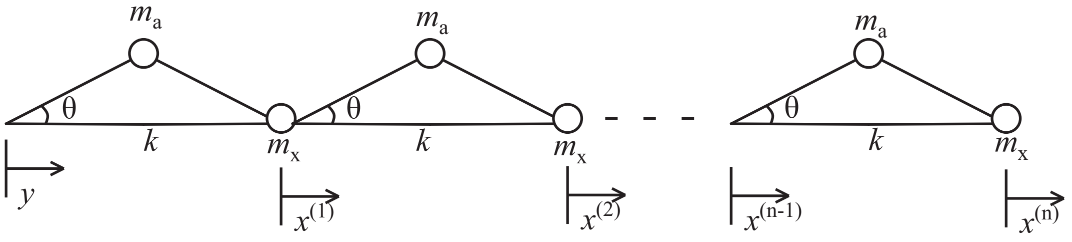

Figure 2.9. 1D Array of Inertial Amplification Mechanisms.

$$\left[m_{\mathrm{a}}\left(\cot^2\theta+1\right)+4m_{\mathrm{x}}\right]\ddot{x}^{(i)}+4kx^{(i)}=m_{\mathrm{a}}\ddot{x}^{(i-1)}\left(\cot^2\theta-1\right)+4kx^{(i-1)} \tag{2.27}$$

$$\left[\left(m_{\mathrm{a}}\left(\cot^2\theta+1\right)+4m_{\mathrm{x}}\right)-m_{\mathrm{a}}\left(\cot^2\theta-1\right)e^{-i\gamma}\right]\ddot{x}^{(i)}+4k\left(1-e^{i\gamma}\right)x^{(i)}=0 \tag{2.28}$$

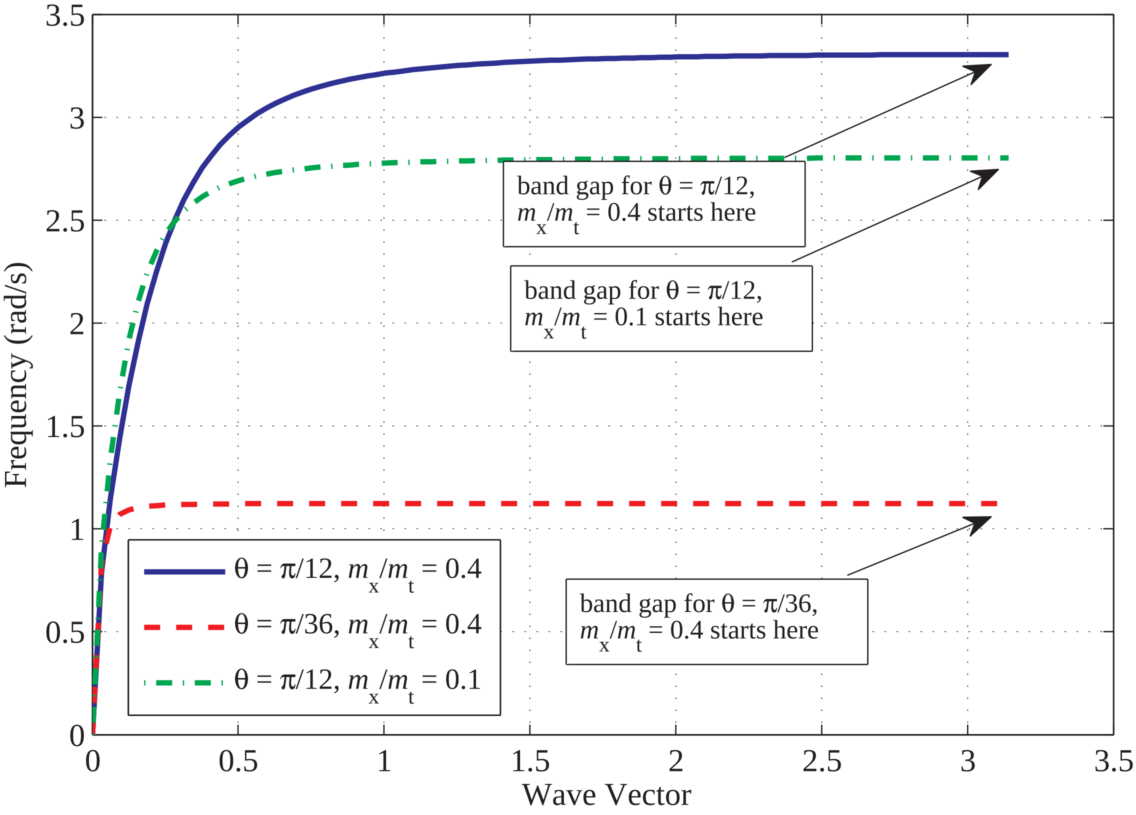

Figure 2.10. Band Structure of Lumped Inertial Amplification Mechanisms for $m_{\mathrm{x}}/m_{\mathrm{t}}=0.4,\theta=\pi/12$, $m_{\mathrm{x}}/m_{\mathrm{t}}=0.4,\theta=\pi/36$, and $m_{\mathrm{x}}/m_{\mathrm{t}}=0.1,\theta=\pi/12$.

By solving Equation 2.28 for γ between 0 and π, band structure of the system is obtained. Band structure of $\theta=\pi/12, m_{\mathrm{x}}/m_{\mathrm{t}}=0.4$, $\theta=\pi/36, m_{\mathrm{x}}/m_{\mathrm{t}}=0.4$, and $\theta=\pi/12, m_{\mathrm{x}}/m_{\mathrm{t}}=0.1$ cases are given in Figure 2.10. As can be seen from Figure 2.10, the system has semi-infinite band gap, and the band gap starts in lower frequencies for smaller θ and smaller m_{x} values. By solving set of equations of motion of the array simultaneously, frequency response of the same cases are given in Figure 2.11 for $n=5$.

By comparing Figure 2.10 with Figure 2.11, one can see that the frequency ranges of the band gap overlap. Besides, from Figure 2.11 it can be seen that the band gap is deeper for larger θ and larger m_{x} values.

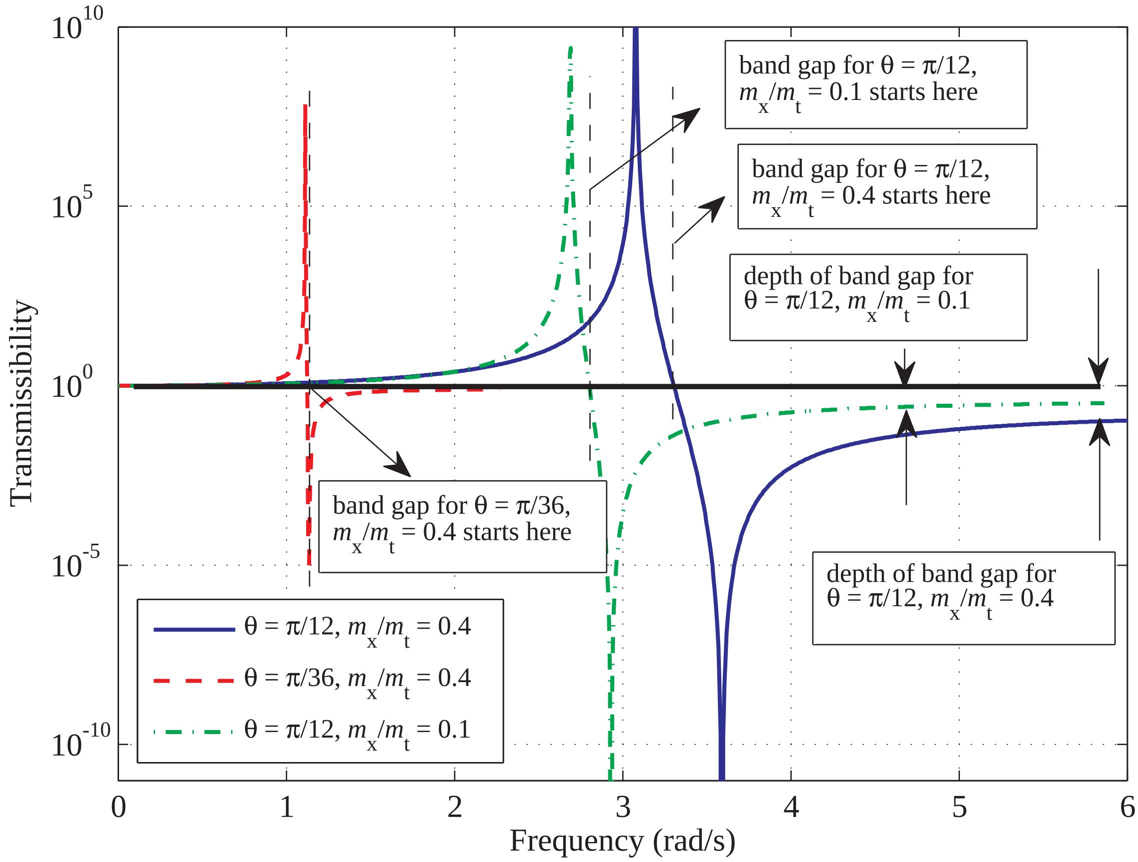

Figure 2.11. Frequency Response of Lumped Inertial Amplification Mechanisms for $m_{\mathrm{x}}/m_{\mathrm{t}} = 0.4, \theta = \pi/12$, $m_{\mathrm{x}}/m_{\mathrm{t}} = 0.4, \theta = \pi/36$, and $m_{\mathrm{x}}/m_{\mathrm{t}} = 0.1, \theta = \pi/12$.

In this thesis, distributed parameter inertial amplification mechanisms are designed. Since they are not composed of rigid elements, mechanisms have more than one natural frequency, and the second natural frequency will set the upper bound of the band gap.

2.2. The Design Problem

The aim of this thesis is to generate a wide and deep band gap in the band structure of the designed 2D periodic structure. The periodic structure is to be composed of 1D distributed parameter model structures. For each 1D structure, the band gap will be created between the first and second natural frequencies, as shown in Figure 2.12.

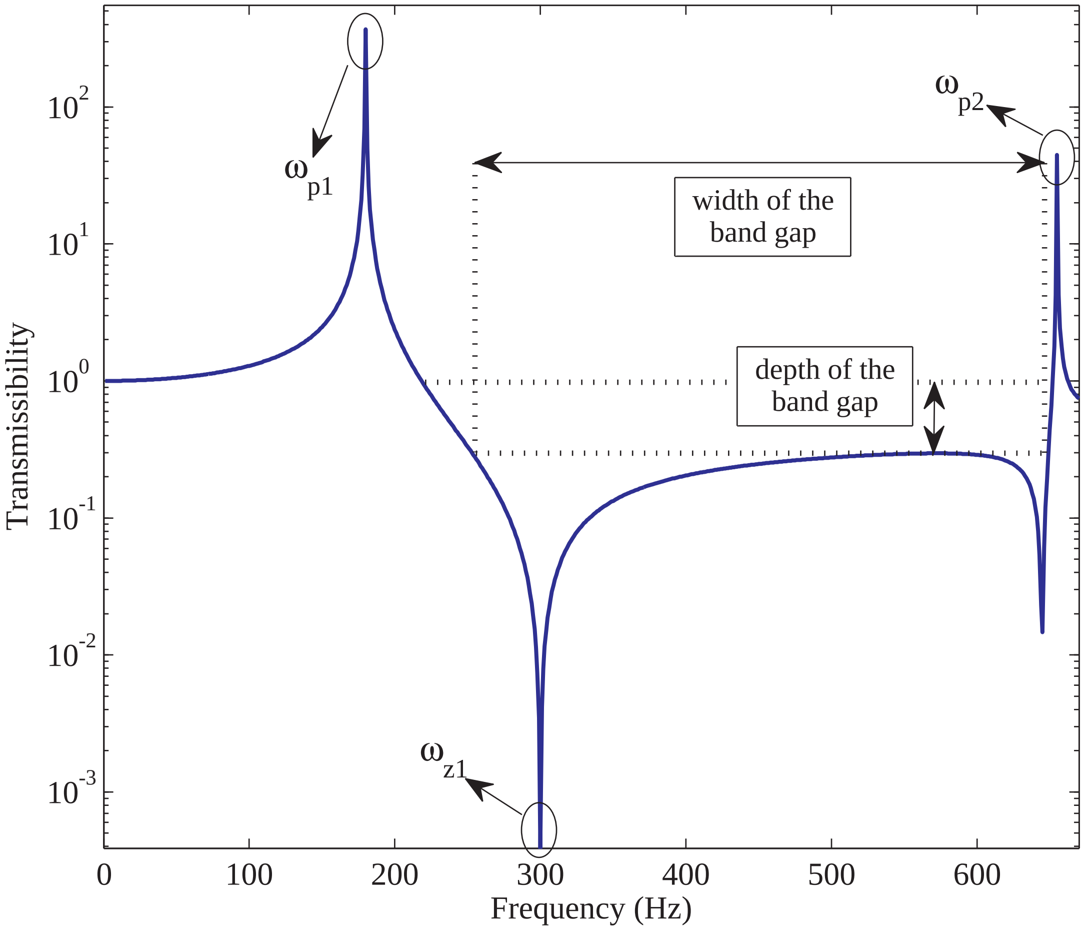

Figure 2.12. Depth and Width of a Band Gap.

The ratio of first natural frequency to the second one, ω_{p1}/ω_{p2}, is aimed to be minimized in order to create a wide band gap. Minimization of the first natural frequency, ω_{p1} , is also aimed in order to lower the frequency ranges of the band gap.

Besides, to make the band gap deeper, $\omega_{\mathrm{p1}}/\omega_{\mathrm{z1}}$ ratio is also minimized.

For the lumped parameter model, transmissibility is given in Equation 2.29.

$$TR = \frac{X(\omega)}{Y(\omega)} = \frac{4k - m_{\mathrm{a}}\left(\cot^2\theta - 1\right)\omega^2}{4k - \left(m_{\mathrm{a}}\left(\cot^2\theta + 1\right) + 4m_{\mathrm{x}}\right)\omega^2} \tag{2.29}$$

In order to find the effect of the first resonance and antiresonance frequencies on the depth of the band gap, the vibration transmissibility is expressed in terms of these frequencies. Both the nominator and the denominator of the Equation 2.29 is divided by $4k$, and the transmissibility is given in Equation 2.30.

$$TR\left(\omega\right) = \frac{1 - \frac{\omega^2}{\omega_{\mathrm{z1}}^2}}{1 - \frac{\omega^2}{\omega_{\mathrm{p1}}^2}} \tag{2.30}$$

The transmissibility becomes smaller as the difference between ω_{p1} and ω_{z1} increases. As can be seen from the Equation 2.25 and Equation 2.26, the point mass attached to the output decreases the resonance frequency whereas it does not affect the antiresonance frequency. Hence, attaching a point mass to the output decreases the transmissibility.

$\omega_{\mathrm{p1}}/\omega_{\mathrm{z1}}$ can also be lowered by reducing the amplification ratio. In other words, for larger θ, $\cot\theta$ is smaller, and the amplification ratio is smaller. Therefore, to create a deep band gap, either a point mass can be attached to the output, or the amplification ratio can be reduced. However, in order to generate a wide band gap in low frequencies, large amplification ratio needed. Thus, there is a trade off between the depth and the width of the band gap.

2.2.1. One-Dimensional Distributed Parameter Model

A distributed parameter model, first mode of which is equivalent to the lumped parameter model, is designed. The sketch of this model is given in Figure 2.13.

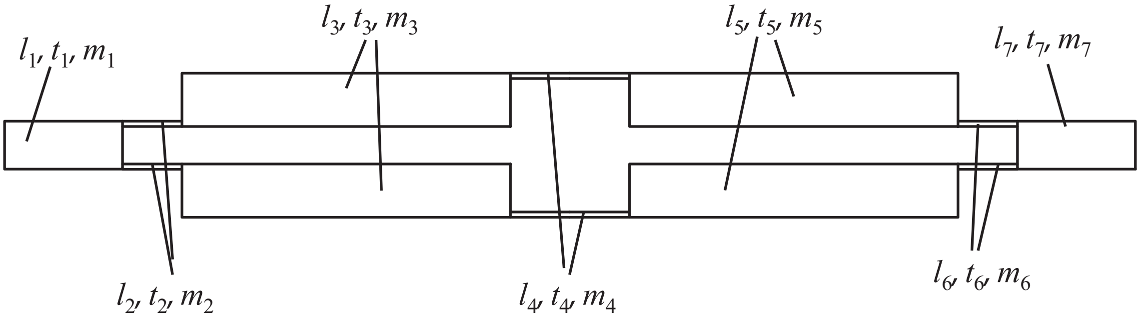

Figure 2.13. Sketch of the Distributed Parameter Model. Here, l_i, t_i and m_i are the length, thickness and mass of the i^{th} section that forms the structure.

First mode shape of the distributed parameter model is given in Figure 2.14. This mode shape is equivalent to the mode shape of the discrete model. To calculate the equivalent k and m_a, the kinetic and potential energy of this mode shape are found.

Thick sections (1, 3, 5, 7) are considered as rigid sections, therefore the change in their potential energy is not taken into account. Besides, thin sections (2, 4, 6) are considered as massless sections, therefore, the change in their kinetic energy is neglected. Potential and kinetic energy expressions are given in Equation 2.31 and Equation 2.32, respectively.

$$V = 4\left(\frac{1}{2}\frac{EI_2}{l_2}\theta^2 + \frac{1}{2}\frac{2EI_4}{l_4}\theta^2\right) \tag{2.31}$$

where I_i is moment of inertia of i^th section, and E is the modulus of elasticity.

$$T = 4\left(\frac{1}{2}\left(\frac{m_3 l_3^2}{12} + m_3\left(\frac{l_3+l_2}{2}\right)^2 + m_3\left(\frac{t_3-t_2}{2}\right)^2\right)\dot{\theta}^2\right). \tag{2.32}$$

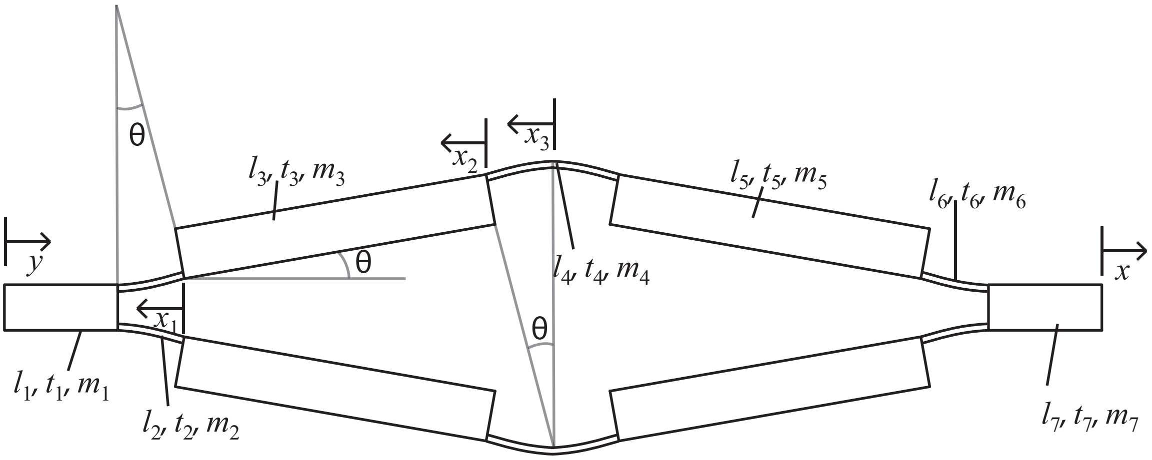

Figure 2.14. First Mode Shape of the Distributed Parameter Model. Here, x_1 and x_2 are the relative axial displacements of the two ends of sections 2 and 3, respectively. x_3 is the relative axial displacement of one end and the middle of section 4.

In order to find the equivalent m_a and equivalent k, the relation between the angular and the axial displacements of the distributed parameter model is found.

Relative axial displacements of the two ends of section 2, section 3 and the half of the section 4 are given in Equation 2.33, Equation 2.34, and Equation 2.35, respectively and shown in Figure 2.14.

$$x_1 = l_2\left(1 - \frac{\sin\theta}{\theta}\right) \tag{2.33}$$

$$x_2 = l_3\left(1 - \cos\theta\right) + \left(t_3 - t_2\right)\sin\theta \tag{2.34}$$

$$x_3 = \frac{l_4}{2}\left(1 - \frac{\sin\theta}{\theta}\right) \tag{2.35}$$

The displacement of one end relative to the other one is given in Equation 2.36.

$$y - x = 2\left(x_1 + x_2 + x_3\right) \tag{2.36}$$

Assuming angular displacements are small, inserting $\sin\theta = \theta$ and $\cos\theta = 1$, into Equation 2.36, the relative displacement of one end with respect to the other one can be found in terms of the angular displacement, as

$$y - x = 2\left(t_3 - t_2\right)\theta. \tag{2.37}$$

Consequently, the equivalent stiffness of the distributed parameter model is found by equating the potential energy expression of the distributed parameter model, Equation 2.31, to that of the lumped parameter one, Equation 2.21. The equivalent stiffness is given in Equation 2.38.

$$k = \frac{EI_2}{l_2\left(t_3 - t_2\right)^2} + \frac{2EI_4}{l_4\left(t_3 - t_2\right)^2} \tag{2.38}$$

Similarly, the equivalent m_a mass of the distributed parameter model is found by equating the kinetic energy expression of the distributed parameter model, Equation 2.32, to that of the lumped parameter one, Equation 2.22. The equivalent m_a is given in Equation 2.39.

$$m_\mathrm{a} = \frac{4}{\left(t_3 - t_2\right)^2\left(1 + \cot^2\theta\right)}\left(\frac{m_3 l_3^2}{12} + m_3\left(\frac{l_3 + l_2}{2}\right)^2 + m_3\left(\frac{t_3 - t_2}{2}\right)^2\right) \tag{2.39}$$

Once k and m_a are found in Equations 2.38 and 2.39, these can be used in Equations 2.25 and 2.26 to determine the first resonance and antiresonance frequencies of the system.

Second natural frequency and mode shape of the one dimensional distributed parameter model is also found analytically. The mode shape is given in Figure 2.15. The relation between θ_1 and θ_2 is geometrically found and given in Equation 2.40.

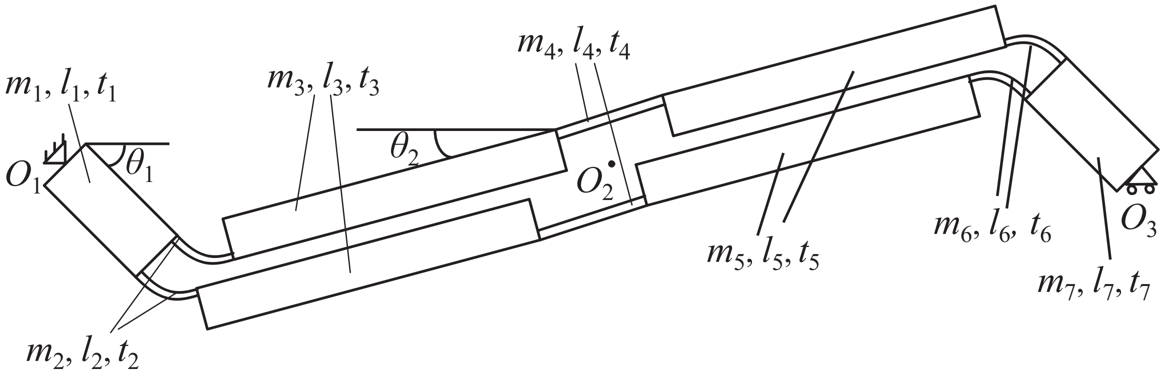

Figure 2.15. Second Mode Shape of the Distributed Parameter Model.

$$\left(l_1 + \frac{l_2}{2}\right)\sin\theta_1 = \left(l_3 + \frac{l_2 + l_4}{2}\right)\sin\theta_2 \tag{2.40}$$

Assuming small displacements ($\sin\theta_1 = \theta_1$, $\sin\theta_2 = \theta_2$), the ratio of θ_2 to θ_1 is given in Equation 2.41.

$$r = \frac{\theta_2}{\theta_1} = \frac{l_1 + \frac{l_2}{2}}{l_3 + \frac{l_2 + l_4}{2}} \tag{2.41}$$

Kinetic energy expression is given in Equation 2.42 by assuming that thin sections (t_2, t_4, and t_6) are massless.

$$T = 2\frac{1}{2}\left(\frac{1}{3}m_1 l_1^2\right)\dot{\theta_1}^2 + 4\frac{1}{2}m_3\left(\frac{l_3^2}{12} + \left(\frac{l_3 + l_4}{2}\right)^2 + d_3^2\right)\dot{\theta_2}^2 \tag{2.42}$$

where d_3 is the distance between the center of section 3 and the symmetry axis of the model, given in Equation 2.43.

$$d_3 = \frac{t_1 + t_3}{2} - t_2. \tag{2.43}$$

Inserting Equation 2.41 into Equation 2.42, Equation 2.44 is obtained.

$$\frac{T_{\mathrm{max}}}{\omega_{\mathrm{p2}}^2} = \left(\frac{1}{3}m_1 l_1^2 + 2r^2 m_3 \left(\frac{l_3^2}{12} + \left(\frac{l_3 + l_4}{2}\right)^2 + d_3^2\right)\right)\theta_1^2. \tag{2.44}$$

Potential energy expression is given in Equation 2.45, by assuming that thick sections(1, 3, 5, and 7) are rigid and section 4 is not flexing.

$$V = 4\frac{1}{2}\frac{EI_2}{l_2}\left(\theta_1 + \theta_2\right)^2. \tag{2.45}$$

Inserting Equation 2.41 into Equation 2.45, Equation 2.46 is obtained.

$$V_{\mathrm{max}} = \left(2\frac{EI_2}{l_2}\left(1 + r\right)^2\right)\theta_1^2 \tag{2.46}$$

Since the total mechanical energy is conserved, maximum potential energy is equal to maximum kinetic energy. Therefore, the second natural frequency is given in Equation 2.47.

$$\omega_{\mathrm{p2}} = \sqrt{\frac{2\frac{EI_2}{l_2}\left(1 + r\right)^2}{\frac{1}{3}m_1 l_1^2 + 2r^2 m_3\left(\frac{l_3^2}{12} + \left(\frac{l_3 + l_4}{2}\right)^2 + d_3^2\right)}} \tag{2.47}$$

2.3. Finite Element Analysis

The three critical frequencies (ω_{p1}, ω_{z1}, and ω_{p2}) that define the depth and width of the band gap in Figure 2.12 can be determined (see Equations 2.25, 2.26, 2.38, 2.39, 2.47) using the approximate analytical model in Section 2.2.1. However, in order to optimize the distributed parameter model, natural frequencies are more accurately calculated by finite element analysis.

2.3.1. Element Mass and Stiffness Matrices

The model is divided into one dimensional beam elements under bending and axial vibrations. Sketch of the element used in the analysis is given in Figure 2.16.

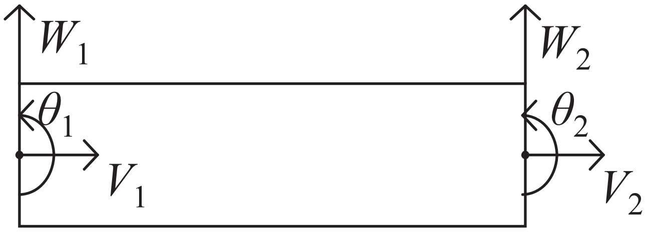

Figure 2.16. Beam Element with Axial and Bending Coordinates.

The element has two nodes, and each of them has three degrees of freedom (axial, lateral, and angular displacement). The axial displacement corresponds to the axial vibrations, and the lateral and the angular displacements correspond to the bending vibrations. The element stiffness and mass matrices are formed by combining the standard axial and bending vibration element stiffness and mass matrices. The element stiffness and mass matrices are given in Equation 2.48, and Equation 2.49.

$$\mathbf{K}_{\mathrm{e}}=\frac{EA}{l}\begin{bmatrix}1&0&0&-1&0&0\\0&0&0&0&0&0\\0&0&0&0&0&0\\-1&0&0&1&0&0\\0&0&0&0&0&0\\0&0&0&0&0&0\end{bmatrix}+\frac{EI}{l^3}\begin{bmatrix}0&0&0&0&0&0\\0&12&6l&0&-12&6l\\0&6l&4l^2&0&-6l&2l^2\\0&0&0&0&0&0\\0&-12&-6l&0&12&-6l\\0&6l&2l^2&0&-6l&4l^2\end{bmatrix}\tag{2.48}$$

$$\mathbf{M}_{\mathrm{e}}=\frac{\rho Al}{6}\begin{bmatrix}2&0&0&1&0&0\\0&0&0&0&0&0\\0&0&0&0&0&0\\1&0&0&2&0&0\\0&0&0&0&0&0\\0&0&0&0&0&0\end{bmatrix}+\frac{\rho Al}{420}\begin{bmatrix}0&0&0&0&0&0\\0&156&22l&0&54&-13l\\0&22l&4l^2&0&13l&-3l^2\\0&0&0&0&0&0\\0&54&13l&0&156&-22l\\0&-13l&-3l^2&0&-22l&4l^2\end{bmatrix}\tag{2.49}$$

As can be seen from Figure 2.13, some segments are not on the symmetry (main) axis of the model. In order to take this eccentricity into account, the mass and the stiffness matrices are multiplied with the transformation matrices formed below.

Effect of the eccentricity on displacements is illustrated in Figure 2.17.

The relation between the axial displacements on the main axis and on the eccentric axis is given in Equation 2.50.

$$x_1 = x_2 - d\theta \tag{2.50}$$

The transformation matrix relating the displacements of the eccentric segment to

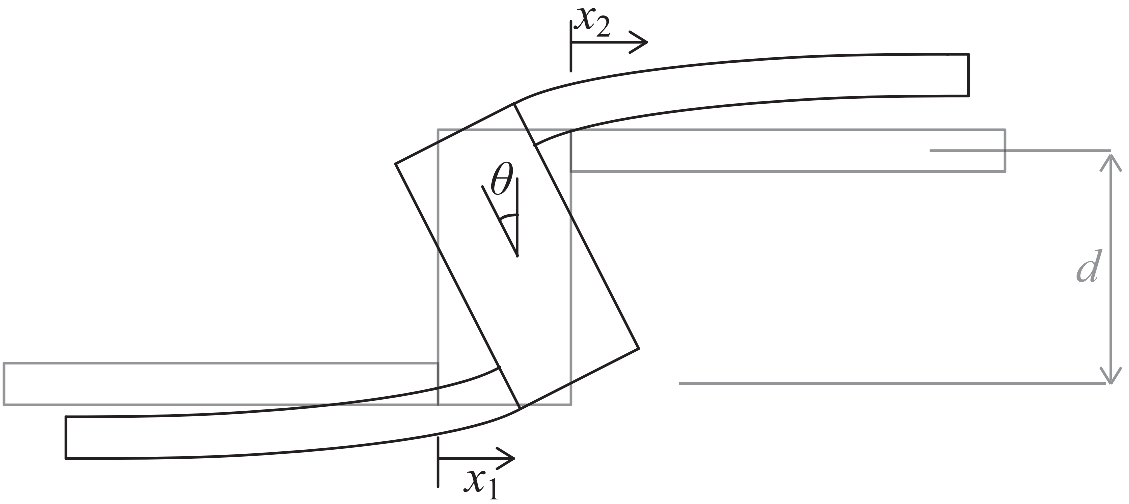

Figure 2.17. Effect of Eccentricity on Displacements.

the main axis is given in Equation 2.51.

$$\mathbf{T}_{\mathrm{d}} = \begin{bmatrix} 1 & 0 & -d & 0 & 0 & 0 \\ 0 & 1 & 0 & 0 & 0 & 0 \\ 0 & 0 & 1 & 0 & 0 & 0 \\ 0 & 0 & 0 & 1 & 0 & -d \\ 0 & 0 & 0 & 0 & 1 & 0 \\ 0 & 0 & 0 & 0 & 0 & 1 \end{bmatrix} \tag{2.51}$$

Effect of the eccentricity on forces and moments is illustrated in Figure 2.18.

The relation between the axial forces and moments on the main axis and on the eccentric axis is given in Equation 2.52 and Equation 2.53.

$$F_2 = F_1 \tag{2.52}$$

$$M_2 = M_1 + F_1 d \tag{2.53}$$

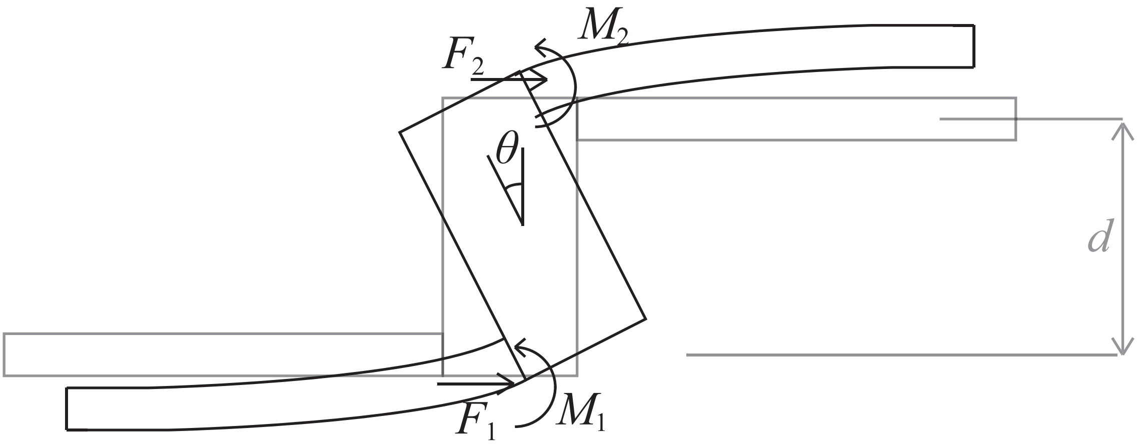

Figure 2.18. Effect of Eccentricity on Forces and Moments.

The transformation matrix relating the forced and moments of the eccentric segment to the main axis is given in Equation 2.54.

$$\mathbf{T}_{\mathrm{f}} = \begin{bmatrix} 1 & 0 & 0 & 0 & 0 & 0 \\ 0 & 1 & 0 & 0 & 0 & 0 \\ d & 0 & 1 & 0 & 0 & 0 \\ 0 & 0 & 0 & 1 & 0 & 0 \\ 0 & 0 & 0 & 0 & 1 & 0 \\ 0 & 0 & 0 & d & 0 & 1 \end{bmatrix} \tag{2.54}$$

Displacements and forces of the eccentric section relative to the local axis are denoted by $\tilde{\mathbf{x}}$ and $\tilde{\mathbf{F}}$, whereas those relative to the main axis are denoted by $\mathbf{x}$ and $\mathbf{F}$. The transformation of the displacements is given in Equation 2.55.

$$\mathbf{x} = \mathbf{T}_{\mathrm{d}}\tilde{\mathbf{x}} \tag{2.55}$$

The transformation of the forces is given in Equation 2.56.

$$\mathbf{F} = \mathbf{T}_\mathrm{f}\tilde{\mathbf{F}} \tag{2.56}$$

$$\mathbf{F} = \mathbf{T}_\mathrm{f}\tilde{\mathbf{F}} = \mathbf{T}_\mathrm{f}\mathbf{K}\tilde{\mathbf{x}} = \mathbf{T}_\mathrm{f}\mathbf{K}{\mathbf{T}_\mathrm{d}}^{-1}\mathbf{x} \tag{2.57}$$

Using the fact that $\mathbf{T}_\mathrm{f} = \left({\mathbf{T}_\mathrm{d}}^{-1}\right)^\mathrm{T}$, the modified stiffness and mass matrices are found and given in Equation 2.58 and Equation 2.59.

$$\mathbf{K}_\mathrm{mod} = \left({\mathbf{T}_\mathrm{d}}^{-1}\right)^\mathrm{T}\mathbf{K}{\mathbf{T}_\mathrm{d}}^{-1} \tag{2.58}$$

$$\mathbf{M}_\mathrm{mod} = \left({\mathbf{T}_\mathrm{d}}^{-1}\right)^\mathrm{T}\mathbf{M}{\mathbf{T}_\mathrm{d}}^{-1} \tag{2.59}$$

2.3.2. Assembly of Element Matrices

In the assembled model, for each subsequent element, the second node of the prior element is the same with the first node of the one after. A sketch of assembly of elements is given in Figure 2.19.

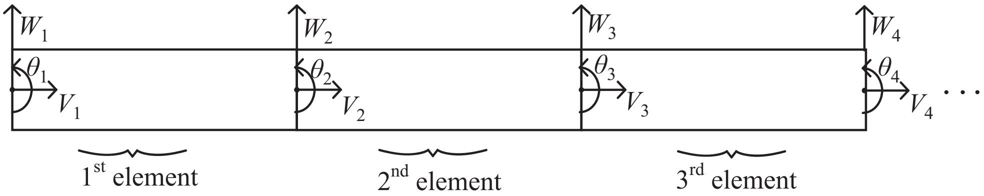

Figure 2.19. Assembly of Elements.

In assembly procedure, terms of element matrices which correspond to the same degree of freedom of the same node are summed up. Since the element matrices are 6x6, for two subsequent element matrices, terms of the last 3x3 portion of the preceding one are summed with the ones of the first 3x3 portion of the following one. Matrix assembly procedure is illustrated in Figure 2.20.

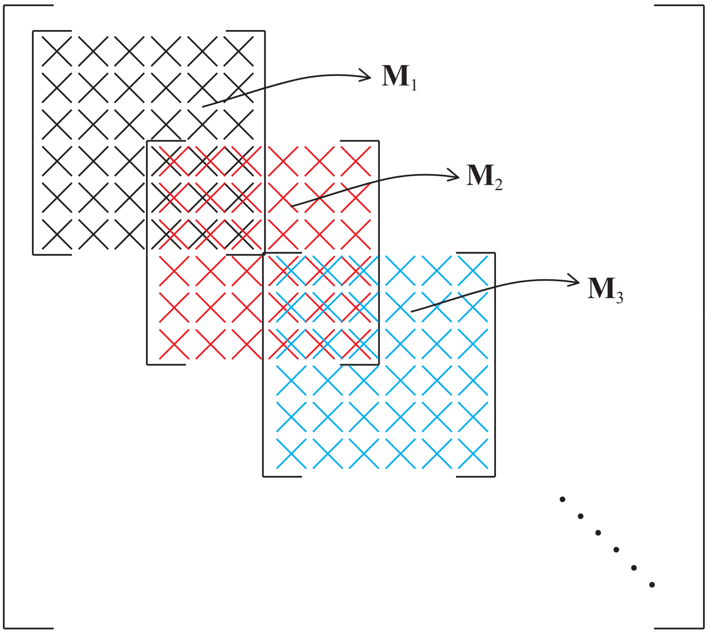

Figure 2.20. Matrix Assembly Procedure.

2.3.3. Branched Model

The distributed model branched into two parts after the first segment and then joined together to the last segment. The model is divided into two models as the main structure and the branch. A sketch of the branched model is given in Figure 2.21.

As can be seen from the Figure 2.21, the last node of the first segment is common both with the first node of the second segment of the main structure and the first node of the branch. Similarly, the node connecting the last segment of the main structure with the one before is common with the last node of the branch. After assembling the global matrices of the main structure and the branch separately in the standard way, the whole model is assembled. The global matrix of the main structure is put

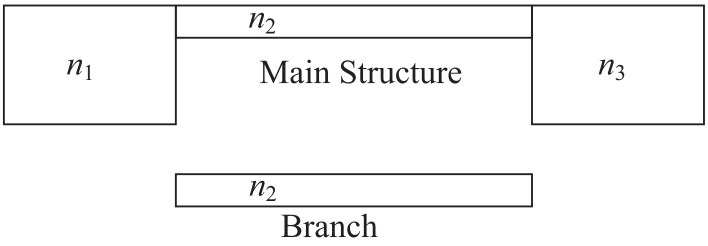

Figure 2.21. A Sketch of the Branched Model. Here, n_i denote the number of elements in the segments.

directly into the general global matrix. Then, terms of the first and the last nodes of the branch are added to the corresponding ones in the global matrix of the main structure. The remaining terms of the global matrix of the branch are placed just after the global matrix of the main structure. Global matrix assembly procedure is illustrated in Figure 2.22.

2.3.4. Boundary Conditions

The distributed parameter model is analyzed under pin - pin roller boundary conditions, as shown in Figure 2.23. In other words, displacement of the first node is prevented in both vertical and horizontal directions, whereas displacement of the last node is prevented only in vertical direction. Vertical and horizontal displacements of the first node correspond to the first and second rows and columns of the global matrices whereas vertical displacement of the last node corresponds to the $(3n_t + 2)^{nd}$ row and column of it. Since these displacements are eliminated, the corresponding rows and columns are deleted. This procedure is illustrated in Figure 2.24.

After applying the boundary conditions, natural frequencies and mode shapes of the model are found via modal analysis.

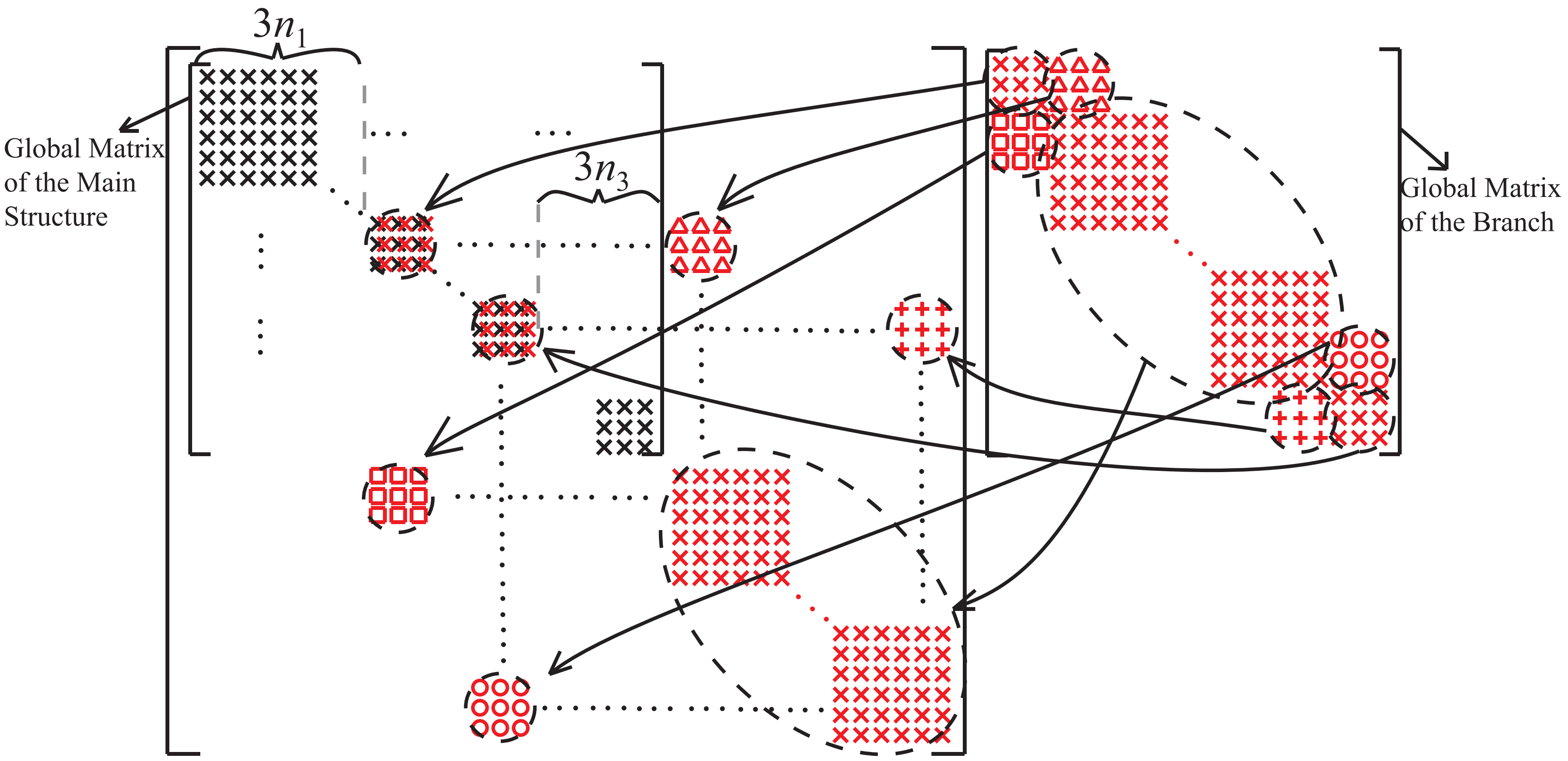

Figure 2.22. Global Matrix Assembly Procedure.

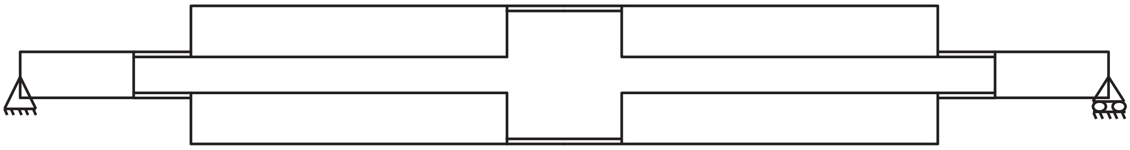

Figure 2.23. Boundary Conditions of the Distributed Parameter Model.

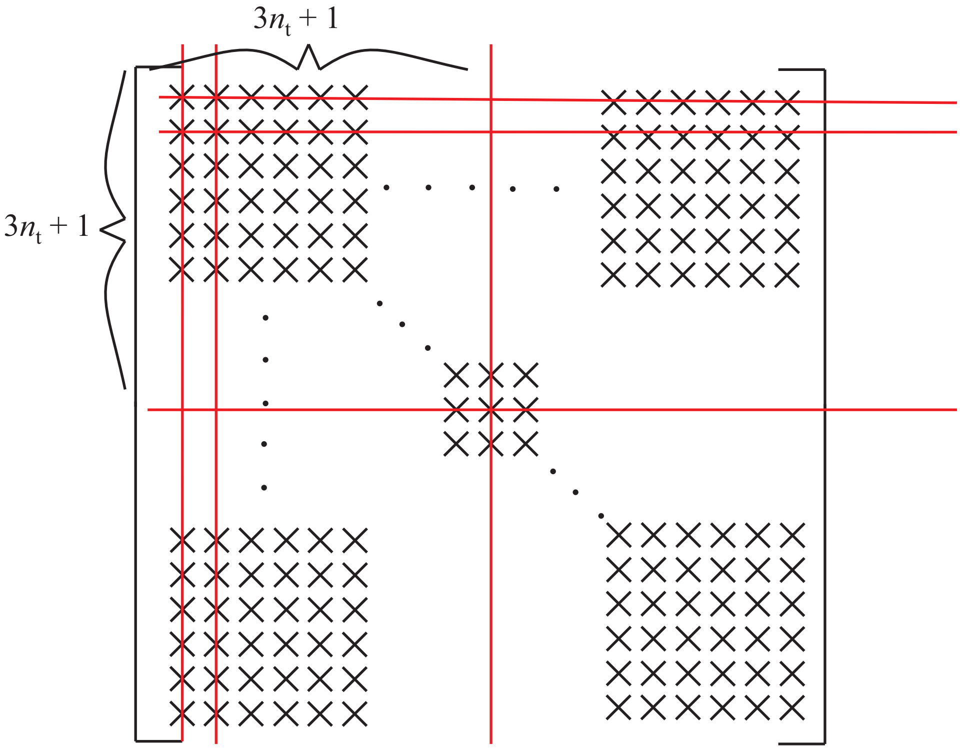

Figure 2.24. Row and Column Deletion for Applying Boundary Conditions.

2.3.5. Modal Analysis

The set of equations of motion of the system in matrix form given in Equation 2.60, where **M** and **K** are global mass and stiffness matrices, respectively.

$$\mathbf{M}\ddot{\mathbf{x}} + \mathbf{K}\mathbf{x} = \mathbf{0}. \tag{2.60}$$

By multiplying the equation with $\mathbf{M}^{-1/2}$ from left, and introducing a new coordinate $\mathbf{q} = \mathbf{M}^{1/2}\mathbf{x}$ with harmonic motion assumption, the eigenvalue problem given in Equation 2.61 is obtained, where, $\mathbf{M}^{1/2}$ is defined as $\mathbf{M}^{1/2}\mathbf{M}^{1/2} = \mathbf{M}$.

$$\left(\tilde{\mathbf{K}} - \omega^2\mathbf{I}\right)\mathbf{q} = \mathbf{0} \tag{2.61}$$

Here, $\tilde{\mathbf{K}}$ is the mass normalized stiffness matrix, and squareroots of its eigenvalues are natural frequencies of the system. Besides, by multiplying eigenvectors of $\tilde{\mathbf{K}}$ with $\mathbf{M}^{-1/2}$ from left, mode shapes are obtained.

2.4. Optimization

The model is optimized in order to create a wide, deep band gap in lower frequency ranges. Minimization of $\omega_{\mathrm{p1}}/\omega_{\mathrm{p2}}$ is selected as optimization parameter in order to make the band gap wider. Besides, $\omega_{\mathrm{p1}}/\omega_{\mathrm{z1}}$ ratio is aimed to be minimized to make the gap deeper, and ω_{p1} is minimized to lower the band gap frequency ranges.

The model is symmetric about the mid-length line perpendicular to the axial direction, $l_1 = l_7$, $l_2 = l_6$, $l_3 = l_5$, $t_1 = t_7$, $t_2 = t_6$, $t_3 = t_5$.

As can be seen from Equation 2.30, the transmissibility decreases with increasing ω_{z1} and decreasing ω_{p1}. For frequencies far from the resonance and the antiresonance frequencies, the transmissibility can be approximated as

$$TR\left(\omega\right) = \frac{\omega_{\mathrm{p1}}^2}{\omega_{\mathrm{z1}}^2}. \tag{2.62}$$

Therefore for smaller $\omega_{\mathrm{p1}}/\omega_{\mathrm{z1}}$ ratio, the band gap is deeper.

From Equation 2.25 and Equation 2.26, it can be seen that point mass attached to the output decreases ω_{p1}, and does not affect ω_{z1} at all. Hence, by increasing the point mass attached to the output, $\omega_{\mathrm{p1}}/\omega_{\mathrm{z1}}$ ratio, so the transmissibility can be reduced.

Another way to reduce the $\omega_{\mathrm{p1}}/\omega_{\mathrm{z1}}$ ratio is to decrease $\cot\theta$. For larger t_3/l_3 ratio, θ is larger, and $\cot\theta$ is smaller.

On the other hand, numerical studies showed that increasing t_3/l_3 ratio also reduces the $\omega_{\mathrm{p2}}/\omega_{\mathrm{p1}}$ ratio, and makes the band gap narrower. In order to make $\omega_{\mathrm{p2}}/\omega_{\mathrm{p1}}$ ratio greater than 2, t_3/l_3 ratio should be at most 0.2. In the optimization study, this ratio is kept fixed at 0.2.

To lower the frequency ranges of the band gap, thickness t_2 is aimed to be minimized. Yet, in order to make this thickness possible to produce with a small tolerance, this thickness is set to 0.5 mm. On the other hand, increasing the length of these sections reduces the overall stiffness of the structure and numerical studies show that smaller t_2/l_2 ratio results in greater $\omega_{\mathrm{p2}}/\omega_{\mathrm{p1}}$ ratio. Yet, t_2/l_2 ratio should be at most 0.2, in order to be able to consider these sections as compliant hinges. Therefore, this ratio is set to 0.2.

Fixed variables: $t_2 = t_4 = t_6 = 0.5$ mm, $l_2 = l_6 = 2.5$ mm, $l_4 = 5$ mm

Free variables: t_1, l_1, t_3

Constraints: $l_3 = l_5 = 5t_3 = 5t_5$, $l_1 = l_7$, $t_1 = t_7$

Optimization toolbox of MATLAB is used where the objective function is minimization of $\omega_{\mathrm{p1}}/\omega_{\mathrm{p2}}$. The lower and upper bounds of the free variables $\begin{bmatrix} t_1 & l_1 & t_3 \end{bmatrix}$ are $\begin{bmatrix} 2 & 8 & 4 \end{bmatrix}$ and $\begin{bmatrix} 6 & 15 & 7 \end{bmatrix}$, respectively.

The optimization study results in $l_1 = l_7 = 12$ mm, $t_1 = t_7 = 4.7$ mm, $l_3 = l_5 = 30$ mm, $t_3 = t_5 = 6$ mm.

Natural frequencies of this structure are calculated by using the approximate analytical model and the finite element model and the results are given in Table 2.1.

Table 2.1. Comparison of Analytical and FEA Natural Frequencies.

	Analytical	FEA
$\omega_{\mathrm{p}1}$	288 Hz	282 Hz
$\omega_{\mathrm{z}1}$	304 Hz	312 Hz
$\omega_{\mathrm{p}2}$	652 Hz	651 Hz

When compared with the finite element analysis results, the error in approximate analytical natural frequencies is at most 2.5%.

The transmissibility of this model is also found by finite element analysis. The model is under pin-roller boundary conditions and a unit axial force and a unit moment are applied from the second node. Since the first node is pinned, it has only θ coordinate. The axial coordinate of the second node, V_2, is the second element of the displacement vector, and the angular coordinate of the same node, θ_2, is the fourth element of it.

$$\mathbf{x} = \begin{bmatrix} \theta_1 \\ V_2 \\ W_2 \\ \theta_2 \\ \vdots \\ \theta_n \\ V_{n+1} \\ \theta_{n+1} \end{bmatrix} \tag{2.63}$$

Therefore, the applied force and moment are placed to the 2nd and the 4th elements of the forcing vector, respectively. Since there is no other force or moment applied to another node, the remaining terms of the forcing vector is zero.

$$\mathbf{f} = \begin{bmatrix} 0 \\ F \\ 0 \\ M \\ 0 \\ 0 \\ \vdots \\ 0 \end{bmatrix} \tag{2.64}$$

For a known forcing vector, nodal displacements can be found by using Equation 2.65.

$$\mathbf{M}\ddot{\mathbf{x}} + \mathbf{K}\mathbf{x} = \mathbf{f} \tag{2.65}$$

Displacement vector is given in Equation 2.66.

$$\mathbf{x} = \left(-\omega^2\mathbf{M} + \mathbf{K}\right)^{-1}\mathbf{f} \tag{2.66}$$

Axial displacement of the last node is the $(3n-1)^{\text{th}}$ element of the displacement vector with $3n$ element. After axial displacement data of the last node is obtained for a range of frequency, in order to find the transmissibility, the whole set is divided by the response at $\omega = 0$. Besides, the same distributed parameter model is analyzed with ABAQUS, a finite element analysis software, and results are compared with those of the finite element model constructed in this thesis. Transmissibilities of the two analyses are plotted in Figure 2.25.

In the finite element model constructed in this thesis, the structure is modeled

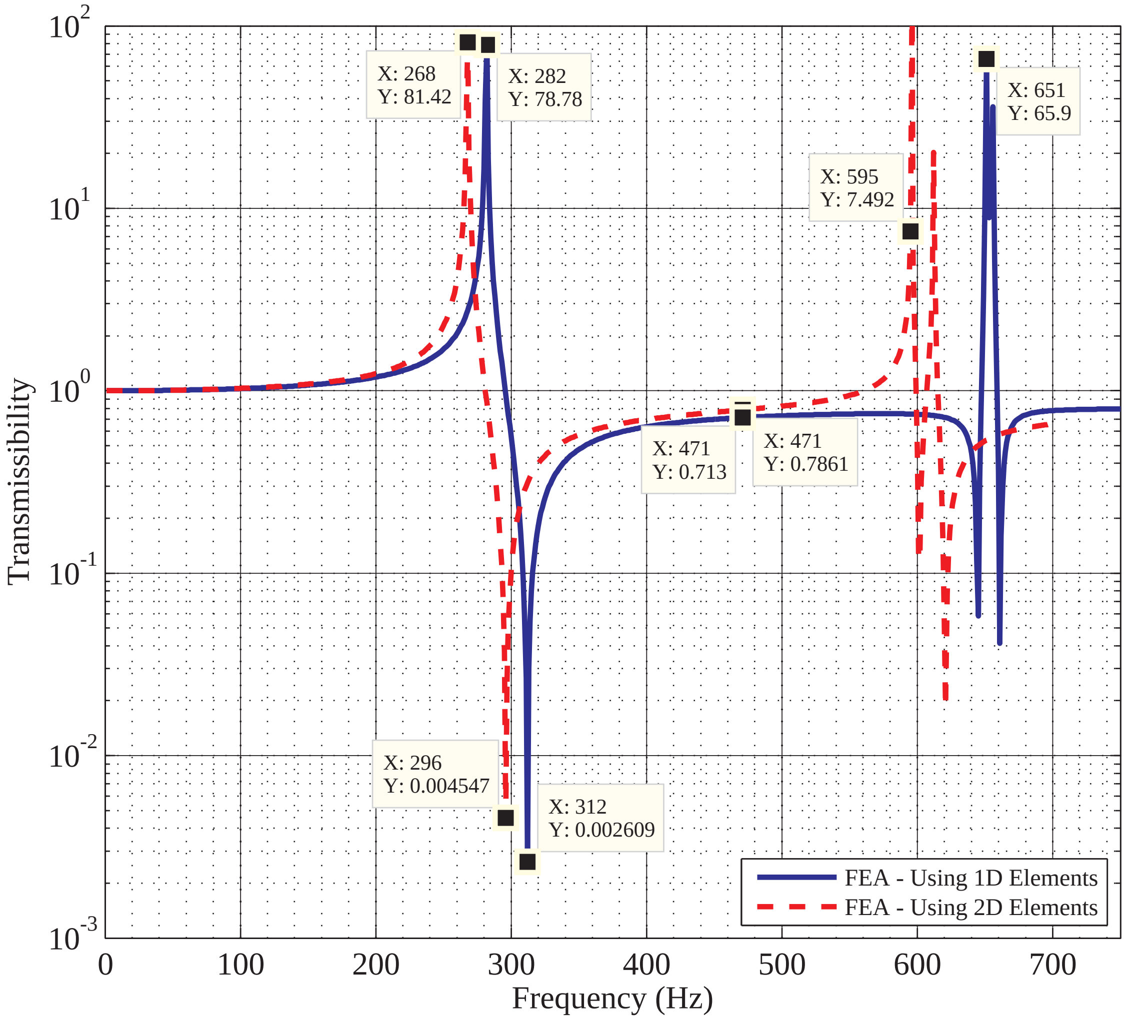

Figure 2.25. Transmissibility of the Optimized 1D Model.

with 1D elements, whereas it is modeled in the software with 2D elements. This difference resulted in $5 - 8\%$ difference in the natural frequencies calculated with the two methods. Our aim is to conduct optimization using $\omega_{\mathrm{p1}}/\omega_{\mathrm{p2}}$ and $\omega_{\mathrm{p1}}/\omega_{\mathrm{z1}}$ ratios. Yet, the difference between the ratio $\omega_{\mathrm{p1}}/\omega_{\mathrm{p2}}$ is about 3% and $\omega_{\mathrm{p1}}/\omega_{\mathrm{z1}}$ ratio is the same for the two analyses. Thus, the finite element model using 1D elements can be used in the optimization study.

2.4.1. Band Structure of the 1D Optimized Model

The band structure of an array of infinite units is constructed, by using Bloch theorem. The theorem relates the displacements of a unit to those of another one. Normally equations of motion of a unit contain terms of the neighboring ones. In order to decouple the equations of motion, Bloch theorem is used.

$$u^{(n+m)} = u^{(n)} e^{i\mathbf{T}m\gamma} \tag{2.67}$$

In Equation 2.67, displacements of $(n+m)^{\text{th}}$ unit are related to those of n^{th} unit. $\mathbf{T}$ is the transformation matrix relating the orientation of the $(n+m)^{\text{th}}$ unit to that of n^{th} one, and γ is the wave vector, defined as $\gamma = 2\pi a d$, where d is the length of the unit and a is the wave number, defined as $a = 1/\lambda$.

In an infinite array of one dimensional units, equations of motion of a specific unit contain displacements of the last node of the previous unit and those of the first node of the following one. In order to decouple the equations from displacements of the neighboring unit cells, Bloch Theorem is used. Since the array is one dimensional, all units are in the same angle, and $\mathbf{T} = 1$. Therefore, global mass and stiffness matrices become a function of only γ. Besides, the minimum physically possible wavelength is $2d$, energy of any higher frequency wave is not transmitted through the lattice. Therefore, the maximum physically possible wave number is $a_{max} = 1/2d$, and $\gamma_{max} = \pi$. By solving the equations of motion for $\gamma = 0 : \pi$, the band structure for the first optimized model is constructed and given in Figure 2.26.

2.4.2. Array of 1D Unit Models

The vibration suppression increases with the number of unit cells in the periodic structure. In order to see the effect of number of unit cells on transmissibility, various number of one dimensional unit cells are assembled. At each assembly point, movement in vertical direction is prevented. For the first optimized unit model, transmissibilities

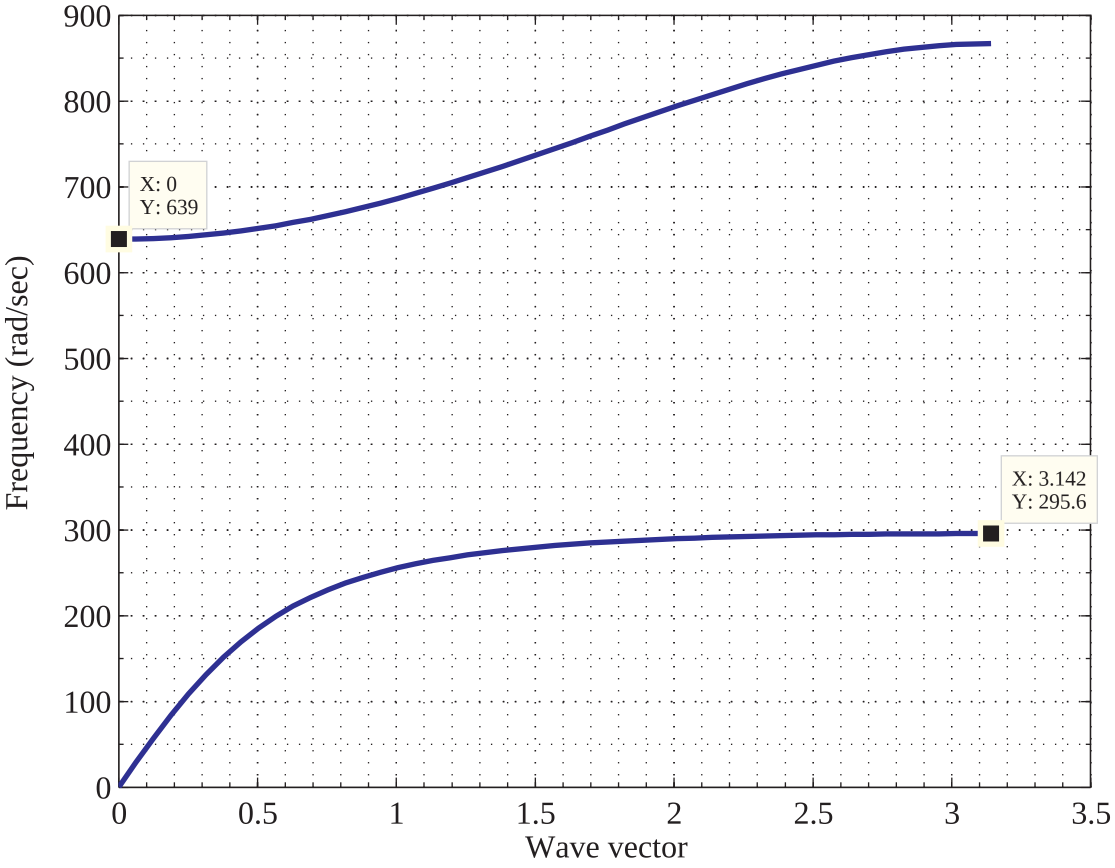

Figure 2.26. Band Structure of the First Optimized 1D Model.

of the array of units are given in Figure 2.27. One can see that the band gap is generated where the transmissibility is below 1, by comparing Figure 2.26 and Figure 2.27. Besides, depth of the band gap is related to the number of unit cells. For 2 1D unit cells, the suppresssion is about 39%, whereas for 4 1D unit cells, it is 8%.

2.4.3. 2D Distributed Parameter Model

After the first 1D branched structure is optimized, these 1D structures are combined to form a 2D periodic structure as shown in Figure 2.28. One can see that the 2D periodic structure is composed of two different size 1D branched structures. The first 1D branched model is decided to be the smaller ones, since t_3 thickness of

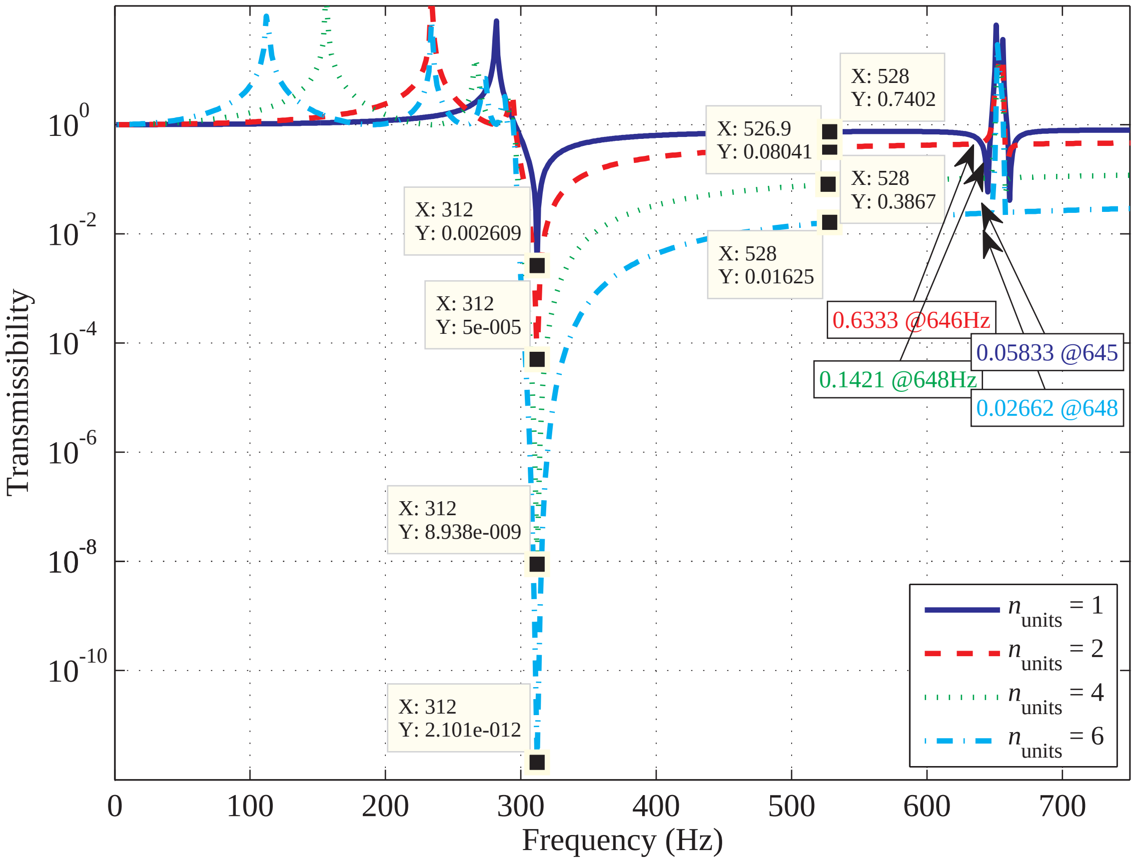

Figure 2.27. Transmissibility of array of units with $n_{\mathrm{units}} = 1$,$n_{\mathrm{units}} = 2$,$n_{\mathrm{units}} = 4$,$n_{\mathrm{units}} = 6$.

the first model is 0.5 mm, which is the minimum thickness for production. Then, the larger ones are optimized so that their ω_{p1}, ω_{p2}, and ω_{z1} frequencies are equal to the corresponding ones of the first optimized model. In the optimization, the objective function is minimization of the sum of squares of the differences between these frequencies $\left(\omega_{\mathrm{p1}} - \omega_{\mathrm{p1}}^{(1)}\right)^2 + \left(\omega_{\mathrm{p2}} - \omega_{\mathrm{p2}}^{(1)}\right)^2$. This sum is minimized, therefore, these frequencies are as close as possible to those of the first model. Besides, t_3/l_3 ratio of the second model is set to that of the first optimized model. Since this ratio is directly related to $\omega_{\mathrm{p1}}/\omega_{\mathrm{z1}}$ ratio, keeping it at the same value makes ω_{z1} of the new model equal to that of the first model, given that they have the same ω_{p1} frequency. The length of the optimized model is also predefined, since, geometrically it has to be exactly $\sqrt{2}$ times the length of the first model.

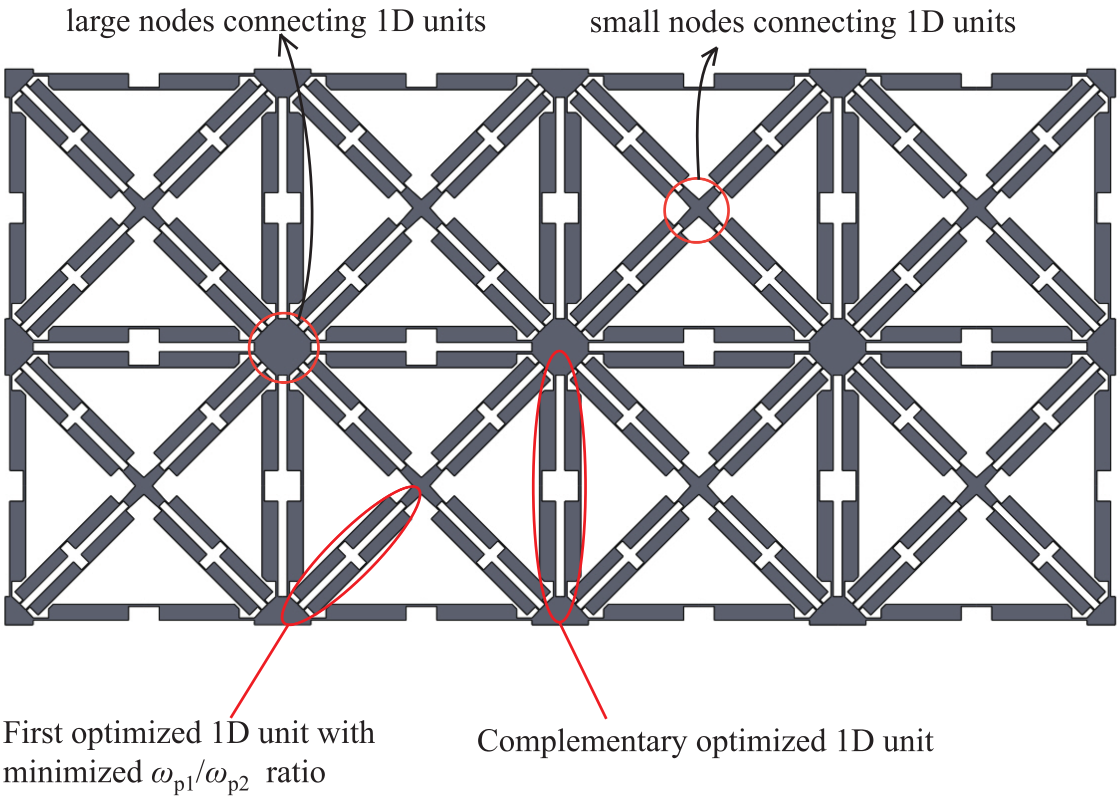

Figure 2.28. Sketch of the 2D Distributed Parameter Model.

Dimensions of the optimized complementary model are given below.

$t_2 = t_4 = t_6 = 1.05$ mm, $l_2 = l_6 = 7.35$ mm, $l_4 = 14.7$ mm, $l_1 = l_7 = 13.5$ mm, $t_1 = t_7 = 6.5$ mm, $l_3 = l_5 = 38.3$ mm, $t_3 = t_5 = 7.66$ mm.

Band structure of the complementary model is given in Figure 2.29. The band gap is generated between 290 Hz - 651 Hz, whereas it is between 296 Hz - 639 Hz for the first optimized model, as shown in Figure 2.26. Thus, when these 1D building blocks are used to form the 2D periodic structure, it is expected to obtain a band gap in 300 Hz - 600 Hz frequency range.

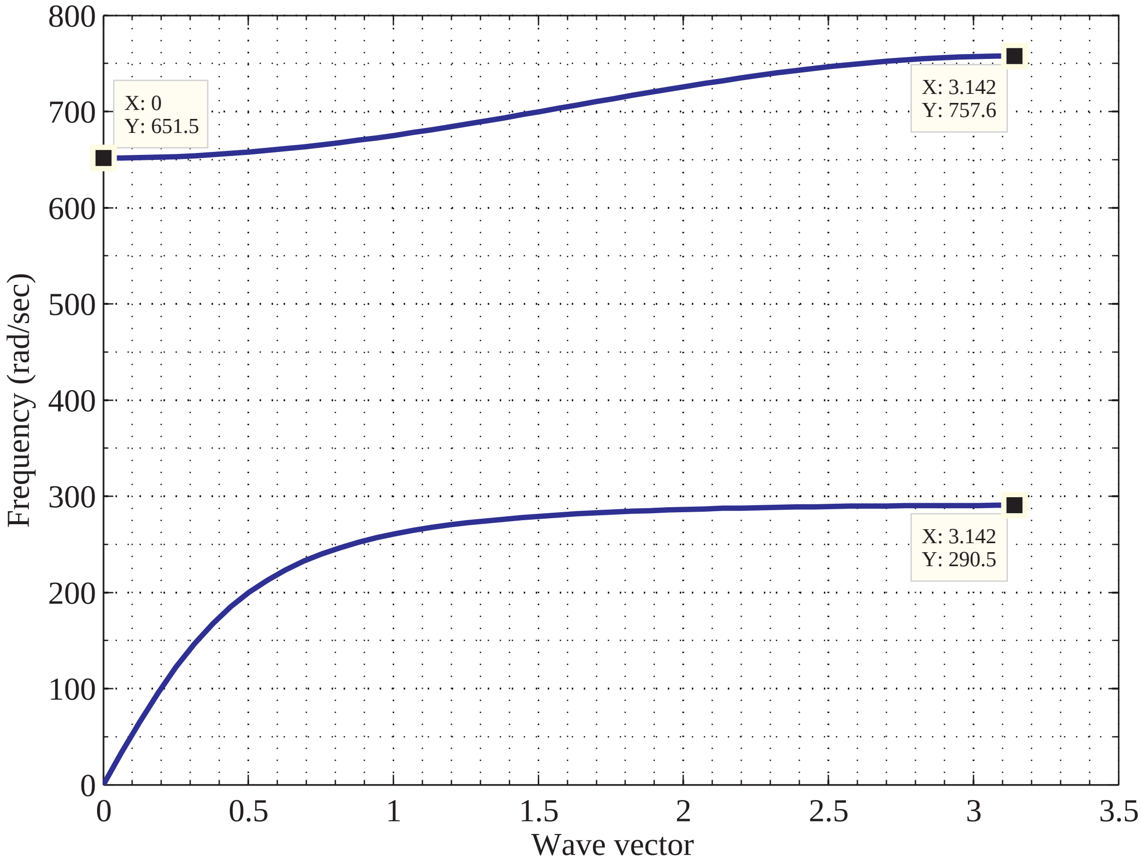

Figure 2.29. Band Structure of the Optimized Complementary 1D Model.

Optimized Complementary 1D structure is analyzed in ABAQUS and frequency response obtained from this analysis and that obtained from 1D finite element analysis are given in Figure 2.30.

2.4.4. Design of Nodes Connecting 1D Units

The nodes connecting 1D units are designed so that the $\omega_{\mathrm{p1}}/\omega_{\mathrm{z1}}$ ratio of the two 1D units is the same. While designing larger nodes, corners of neighboring 1D units are connected directly. Then, area of this large node is found geometrically, and mass of it is calculated. As shown in Figure 2.28, this node can be excited in vertical, horizontal and diagonal directions. When excited in horizontal or vertical directions,

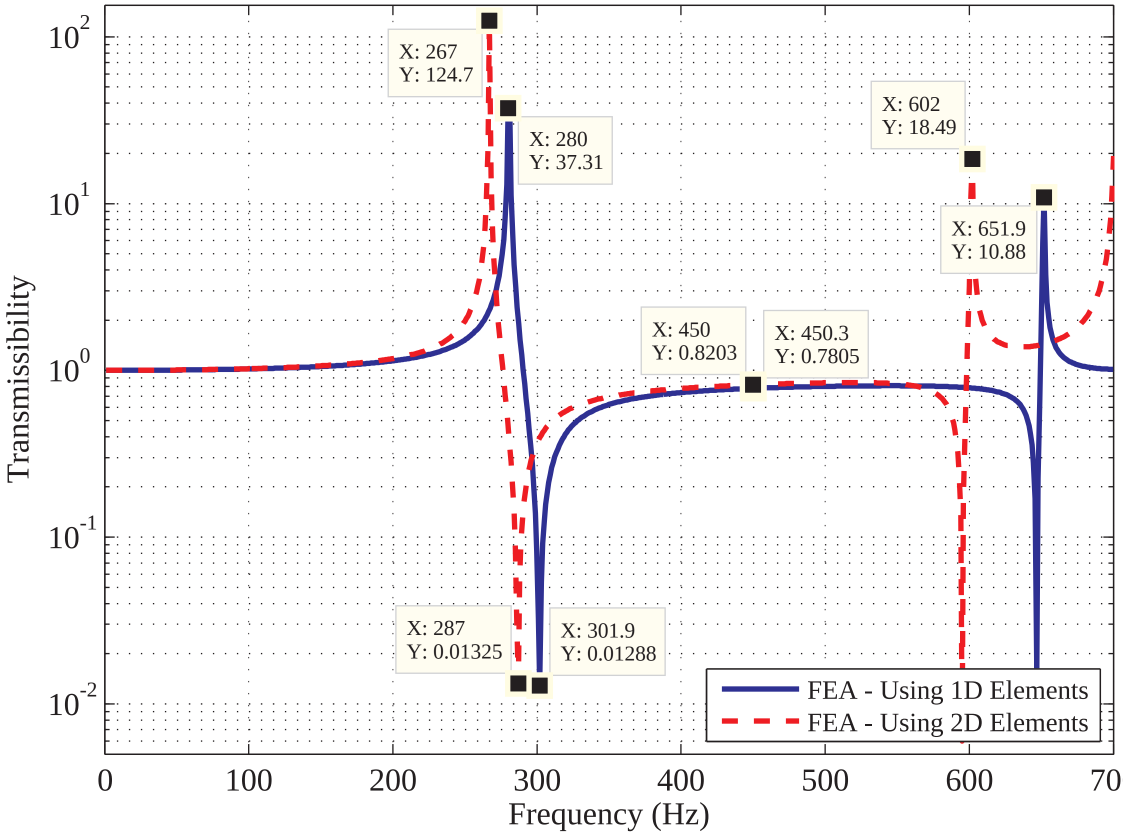

Figure 2.30. Transmissibility of the Optimized Complementary 1D Model.

it is effectively connected to two large 1D units, since they are oriented in excitation direction, and to two small 1D units, since there are 4 of them making 45° with the excitation direction. When excited in diagonal direction, it is effectively connected to two small 1D units, since they are oriented in excitation direction, and to two large 1D units, since there are 4 of them making 45° with the excitation direction. Therefore, when excited in any direction, the large node is effectively connected to two small 1D units and two large 1D units. A similar argument holds for the small nodes, as well. However, as there are no large 1D units attached to a small node, when excited in any direction, the small node is effectively connected to two small 1D units. Therefore, the mass ratio of the two nodes should be equal to the ratio $2m_1/\left(2m_1 + 2m_1'\right)$ where, m_1 is mass of the first segment of the small 1D unit, and m_1' is mass of the first segment of the large 1D unit. Mass of the small node is found from this relation, and its geometry is designed accordingly.

3. NUMERICAL AND EXPERIMENTAL ANALYSIS OF THE 2D MODEL

3.1. Finite Element Analysis

2D model designed in Section 2.4.3, is analyzed in Finite Element Analysis software, ABAQUS. First, modal analysis is conducted in order to find the natural frequencies and mode shapes. Then, frequency response of the model is found.

3.1.1. Modal Analysis

The mesh of the 2D model is given in Figure 3.1. Each segment has 4-6 elements along thickness. The element type is CPS4I, which is a 4-node, quadratic, plane stress element.

The model is subjected to pin boundary condition at left-top corner and pin-roller boundary condition at left-bottom corner, as shown in Figure 3.1.

When modal analysis is conducted on the 2D model, 43 resonance frequencies are obtained up to 276 Hz. However, the next resonance frequency is at 611 Hz. 43$^{\mathrm{rd}}$ and 44$^{\mathrm{th}}$ mode shapes are given in Figure 3.2 and Figure 3.3, respectively. As can be seen from these mode shapes, 1D building blocks are excited in their first natural frequency at $\omega_{\mathrm{p}43} = 276\mathrm{Hz}$ and in their second natural frequency at $\omega_{\mathrm{p}44} = 611\mathrm{Hz}$. The band gap is expected to be generated between these two natural frequencies.

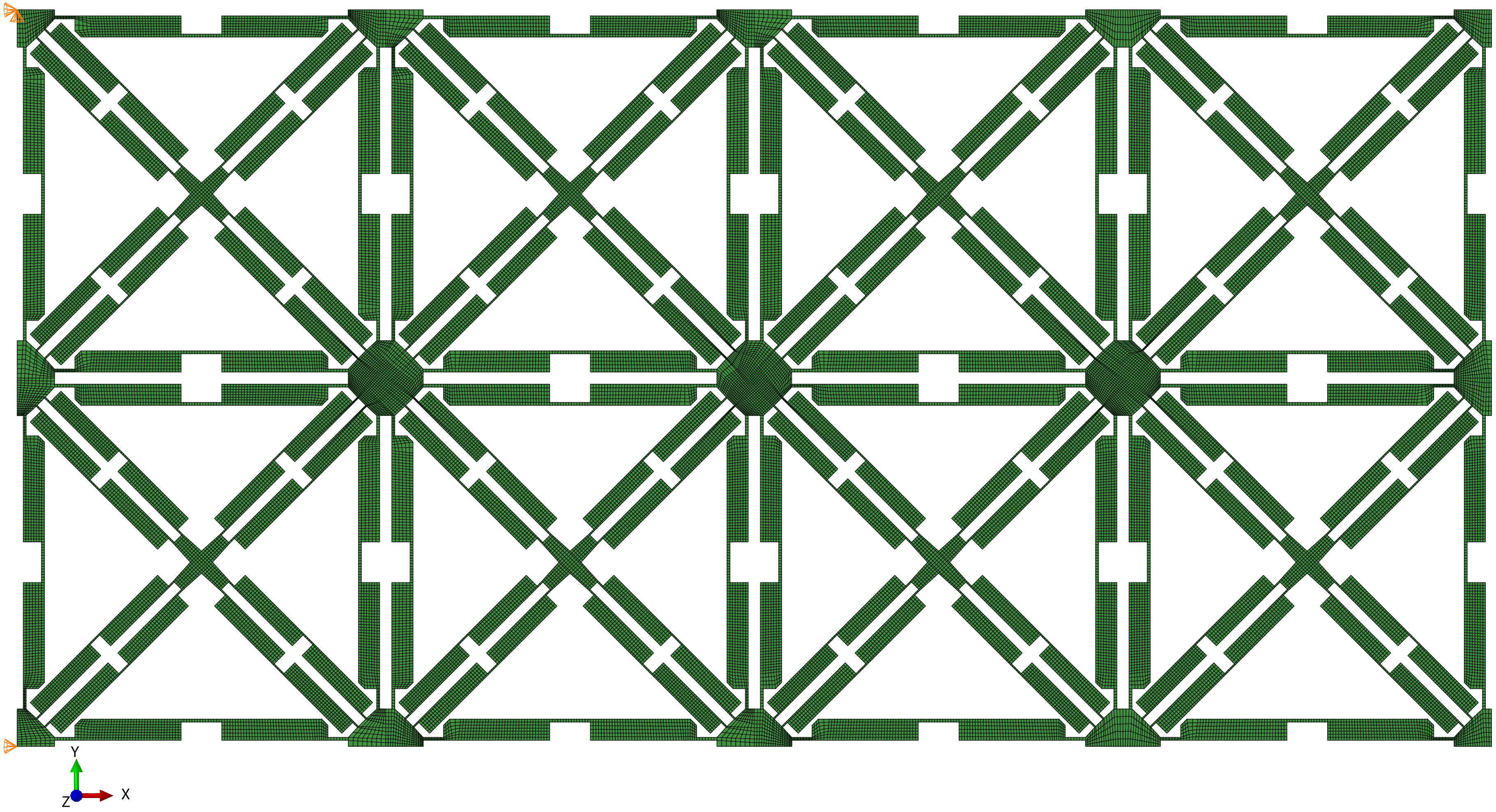

Figure 3.1. Finite Element Mesh of the 2D Model.

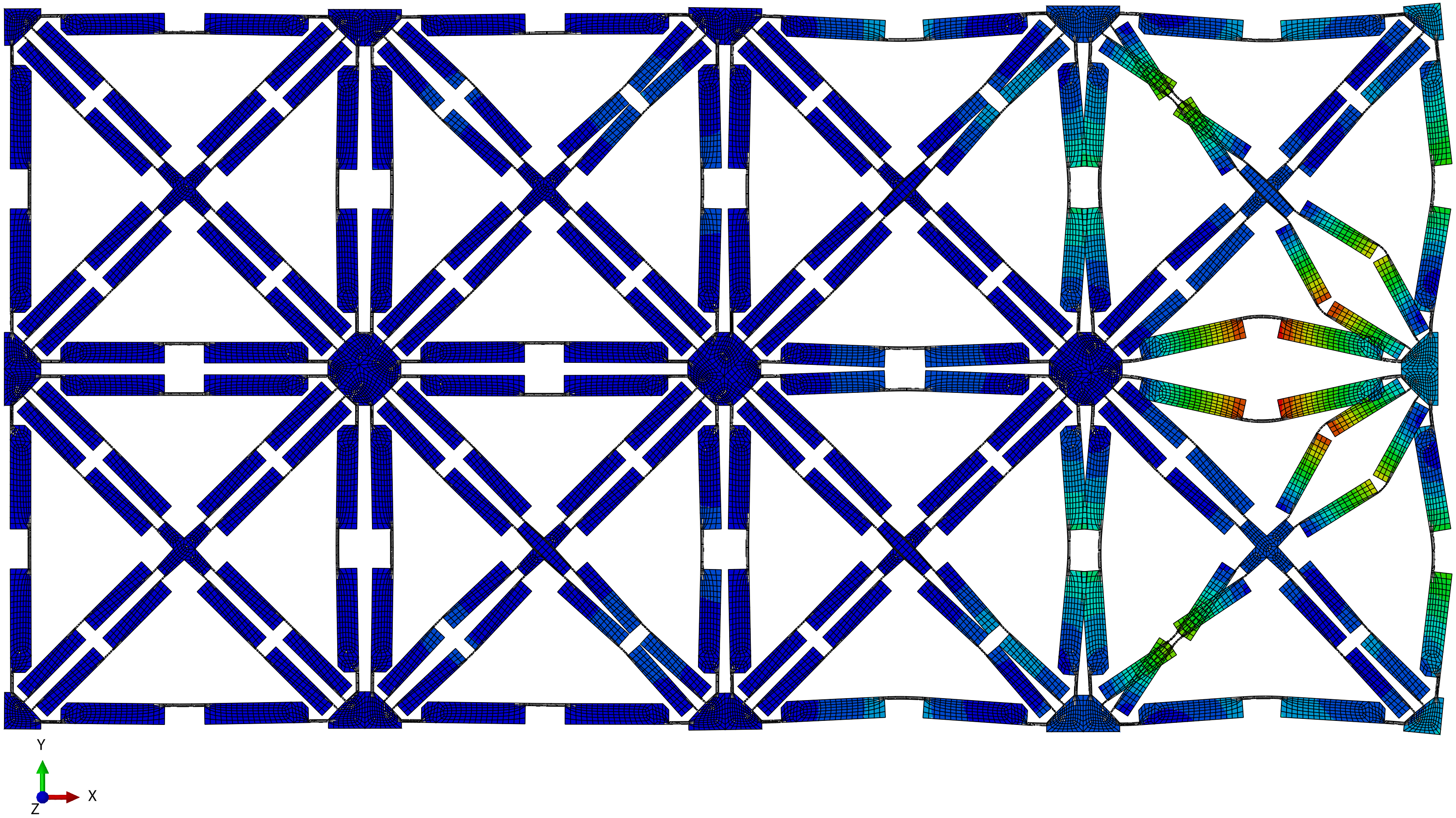

Figure 3.2. 43rd Mode Shape for the 2D Optimized Model (276.4 Hz).

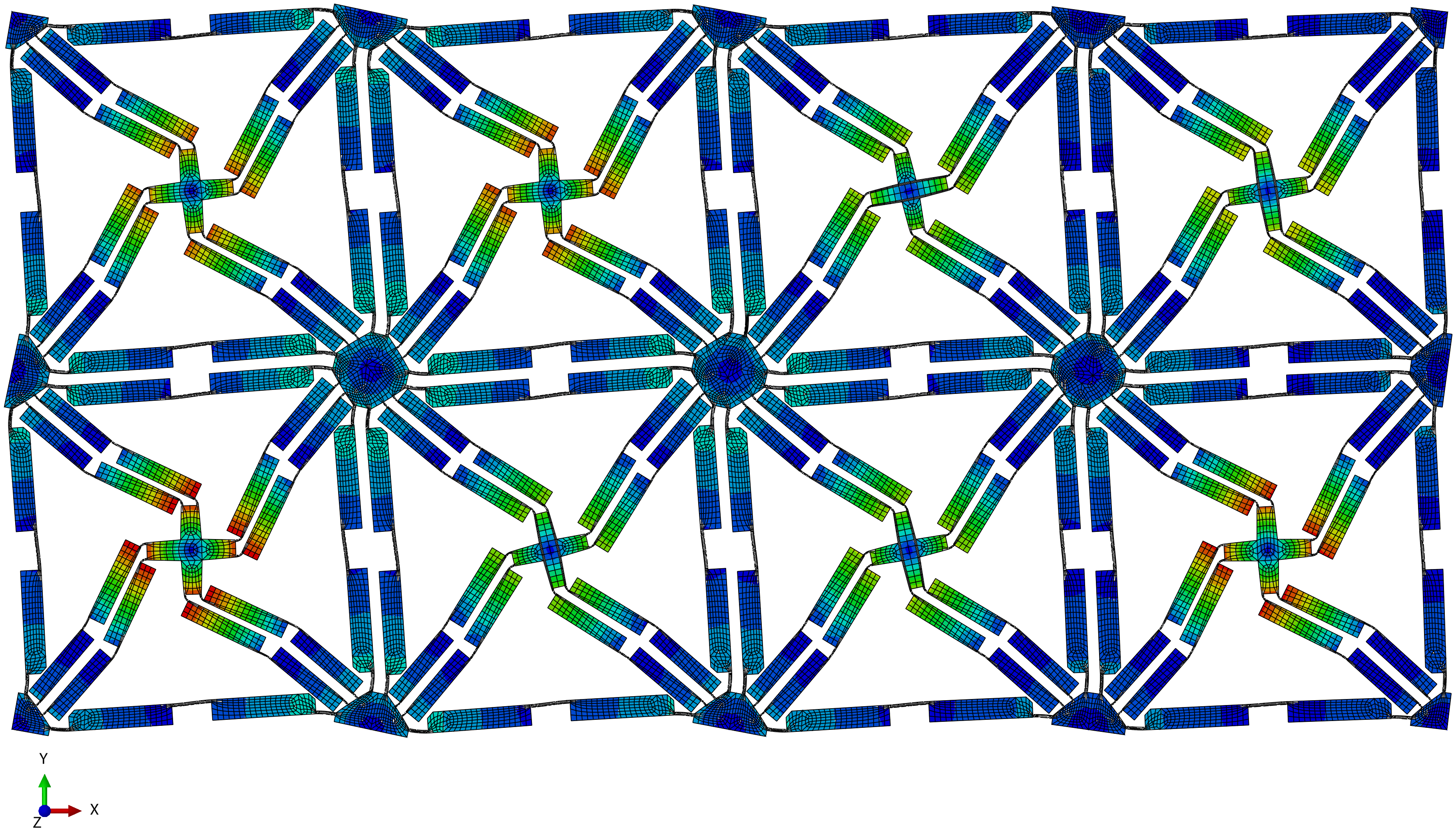

Figure 3.3. 44$^{\text{th}}$ Mode Shape for the 2D Optimized Model (611 Hz).

3.1.2. Frequency Response

Frequency response of the same model with the same mesh and the same boundary conditions is found. Excitation is given from midpoint of the left edge and output displacement is calculated at the midpoint of the right edge. Thus, transmissibility of 4 unit cells is found, given in Figure 3.4. By comparing this result with the response of 1D array of elements, one can see that for the same number of unit cells, 2D model results in lower transmissibility. As can be seen from Figure 2.27, transmissibility of 1D array with 4 unit cells is about 8%, whereas for the same number of unit cells in 2D assembly, transmissibility is about 2%. Since, each unit cell has more number of neighboring ones, interactions with them reduces energy of the propagating wave more in 2D case and the model results in a better response. Besides, by comparing Figure 2.27 with Figure 3.4, one can see that the band gap frequencies overlap.

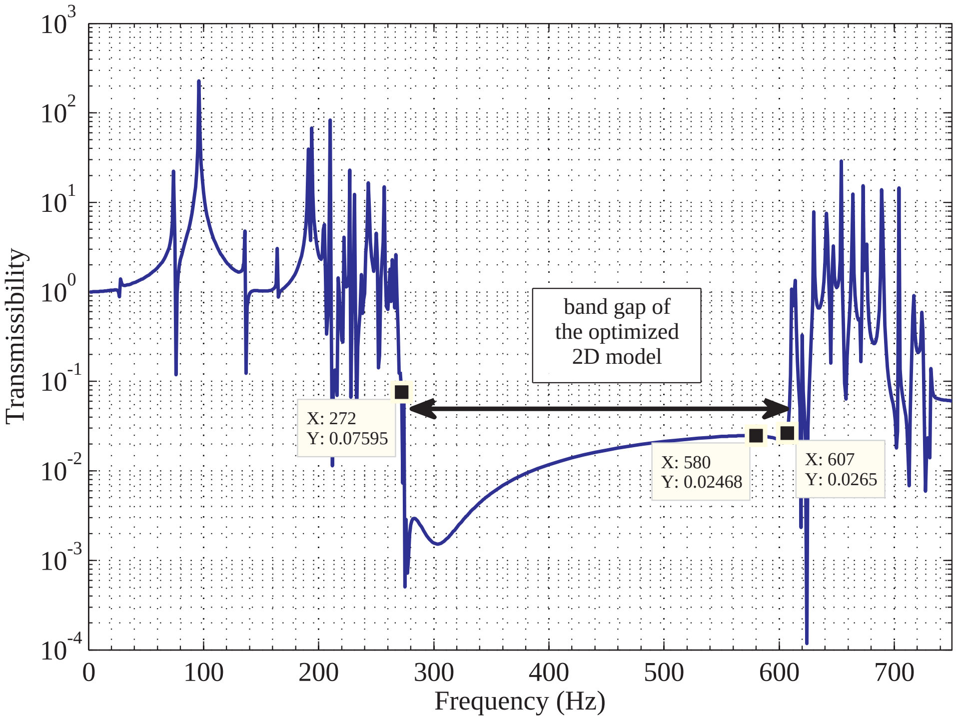

Figure 3.4. Frequency Response of the Optimized 2D Model. Only 2.5% of the Input Vibration is Transmitted to the Output End in the Frequency Range 272 Hz - 607 Hz.

During production phases, small deviations might occur in dimensions. These deviations are critical for thin sections (Section 2, 4 and 6) of the both 1D unit models. In order to find the effect of these deviations on natural frequencies and frequency response, Finite Element Analysis is conducted on models with different standard deviations in t_2 dimensions. As can be seen from Figure 3.5, the band gap is wider for smaller standard deviation. For Standard Deviation $= 10\mu$m, only 2.4% of the input vibration is transmitted to the output end in the frequency range 281Hz – 619Hz. For Standard Deviation $= 30\mu$m, only 2.6% of the input vibration is transmitted to the output end in the frequency range 282Hz – 614Hz. For Standard Deviation $= 100\mu$m, only 2.4% of the input vibration is transmitted to the output end in the frequency range 293Hz – 587Hz.

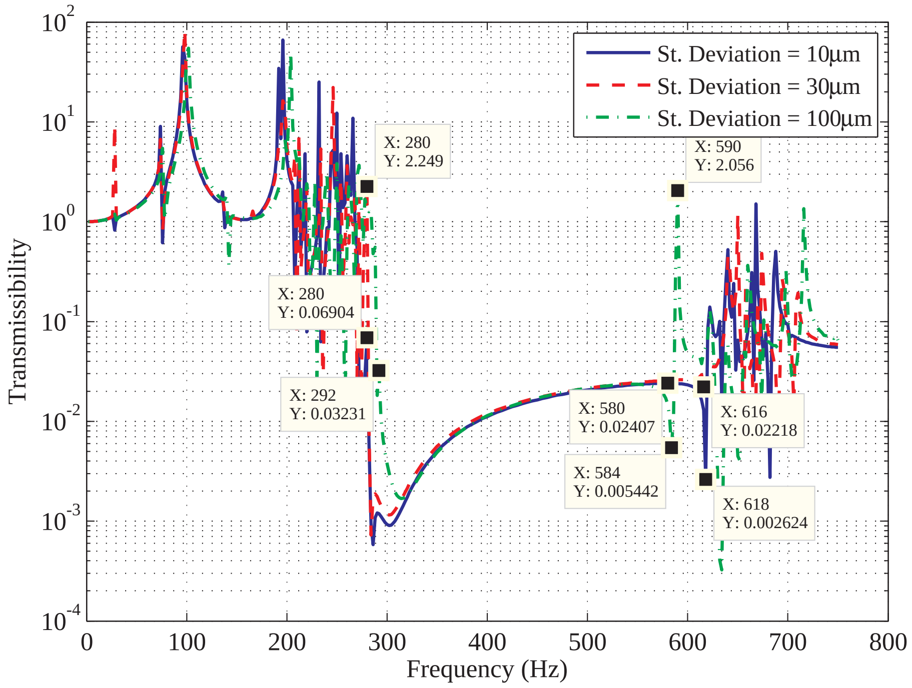

Figure 3.5. Effect of Deviations in Dimensions on the Frequency Response of the 2D Model.

Damping affects the sharpness of peaks, hence the frequency response of the system. When there is no additional damper in the system, the only damping source is the material damping. For different structural damping values, FEA is conducted on the 2D model in order to find the effect of damping on the frequency response. As can be seen from Figure 3.6, resonances and antiresonances become smoother for larger damping values.

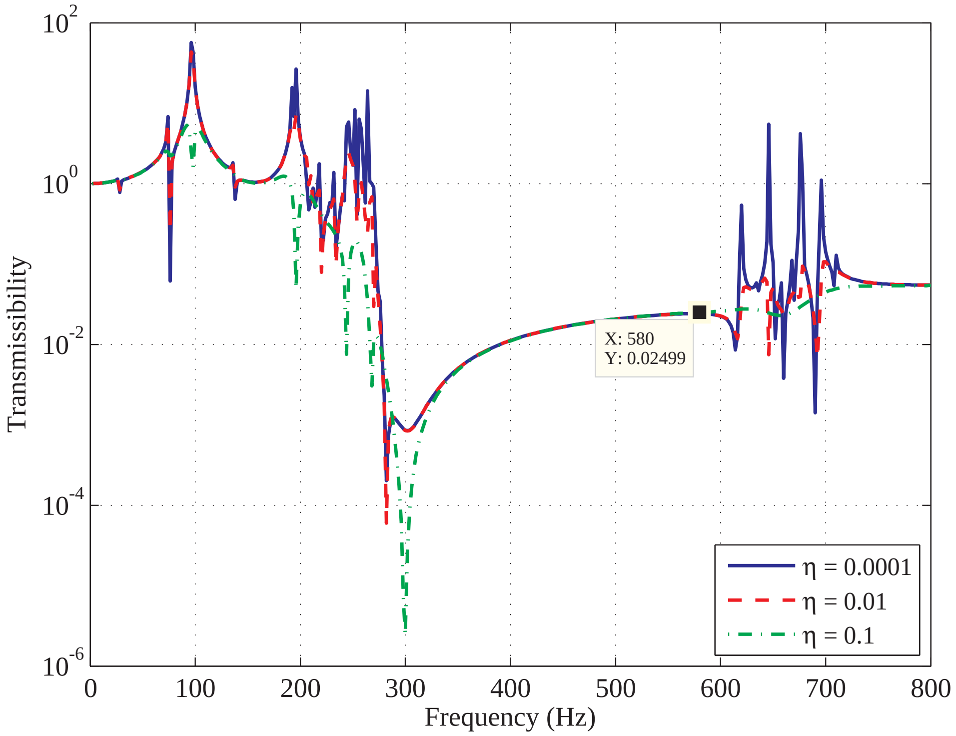

Figure 3.6. Effect of Damping on the Frequency Response of the 2D Model.

3.2. Experimental Results

The two-dimensional optimized model given in Figure 2.28 is produced from a 25 mm thick plate of AISI P20(Commercial Name: Impax Supreme, $\rho = 7800$ kg/m^3, $E = 205$ GPa, $\sigma_y = 900$ MPa, $\sigma_u = 1020$ MPa) steel. To produce the structure, a high strength steel is selected so that the material damping is low. As a result, the resonances and the antiresonances of the structure can easily be seen. Wire EDM(Electrical Discharge Machining) method is used since it provides small dimensional tolerances. Stress relieving heat treatment is made before the cutting process.

3.2.1. Production

After a market search, two wire EDM providers are selected for their relatively good performance and low costs. In order to compare their performances and select one for production of the two-dimensional model given in Figure 2.28, both providers are asked to produce one first 1D optimized unit model, one 1D complementary optimized unit model, and one square unit cell (CAD model of the square unit cell can be seen in Figure 3.7).

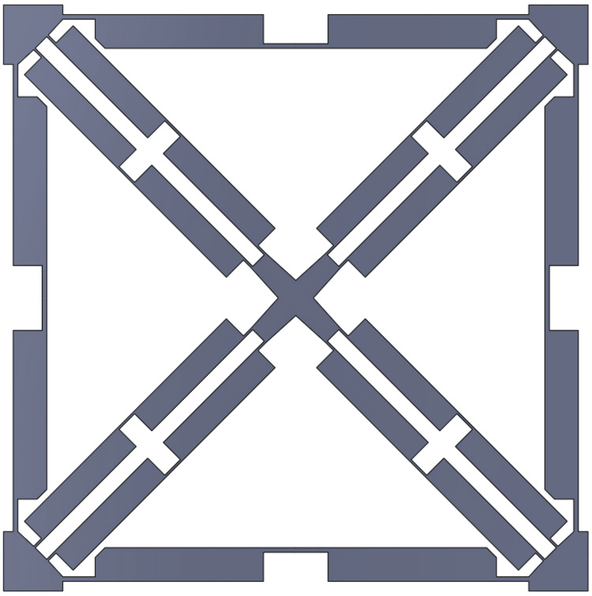

Figure 3.7. Square Unit Cell of the 2D Optimized Model. Corners of the 1D Complimentary Unit are Cut to Eliminate Interference with the First 1D Optimized Models.

First 1D optimized models, 1D complementary models and square unit cells produced by two providers are given in Figure 3.8.

Since thickness of section 2(which is equal to that of section 4 and 6) is very small and critical (highly affects the natural frequencies), t_2 dimensions of the prototypes are compared. For each prototype, all t_2 measurements are recorded and their maximum,

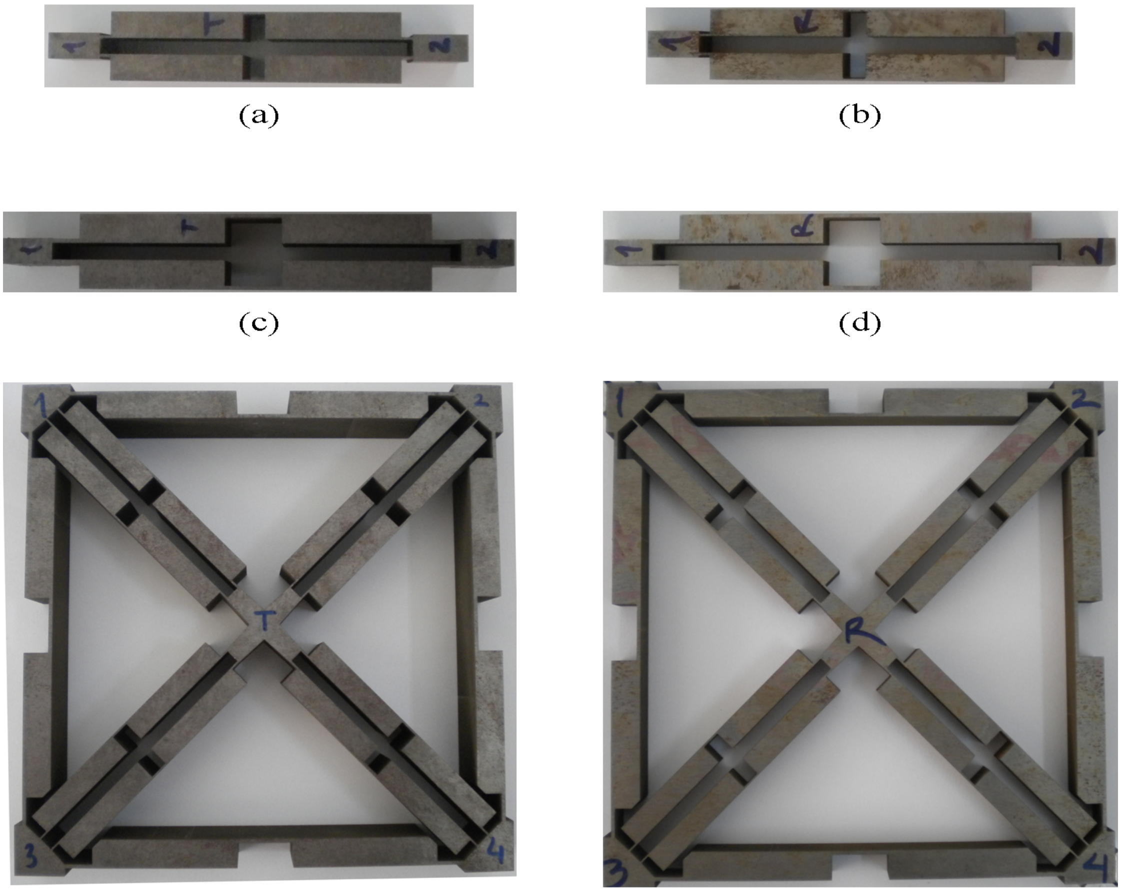

(a)
(b)
(c)
(d)
(e)
(f)

Figure 3.8. Prototypes Produced by the Two Providers. a)First Optimized 1D Model (Provider 1), b) Complementary 1D Model (Provider 1), c) Square Unit Cell (Provider 1), d)First Optimized 1D Model (Provider 2), e) Complementary 1D Model (Provider 2), f) Square Unit Cell (Provider 2).

minimum, average and standard deviation values are calculated. Measurements of the first optimized unit model, and the complementary optimized unit model are given in Table 3.1, and Table 3.2, respectively. Ideally, in the first model, t_2 should be 500 μm, and in the second one, t_2 should be 1050 μm. Yet, for the first one, Provider 1 has average value 487.5 μm with standard deviation 7.5 μm, whereas average value of Provider 2 is 463.3 μm with standard deviation 7.8 μm. Similarly, for the second model, average of Provider 1 is 1045 μm with standard deviation 8 μm, whereas that of Provider 2 is 1040 μm with standard deviation 7.8 μm. Therefore, average of Provider 1 is closer to the ideal t_2 dimension with a similar amount of standard deviation.

Table 3.1. t_2 Dimensions of the First 1D Optimized Model (in μm).

	Provider 1	Provider 2
	480	460
	490	470
	480	460
	480	460
	500	470
	490	460
	480	450
	500	460
	490	480
	480	460
	490	460
	490	470
Minimum	480	450
Maximum	500	480
Average	487.5	463.3
St. Deviation	7.5	7.8

Similarly, t_2 dimensions of the first 1D optimized and 1D complementary models

Table 3.2. t_2 Dimensions of the 1D Complementary Optimized Model (in μm).

	Provider 1	Provider 2
	1050	1050
	1060	1030
	1050	1050
	1040	1030
	1050	1040
	1050	1040
	1040	1040
	1040	1040
	1050	1050
	1040	1040
	1030	1030
	1040	1040
Minimum	1030	1030
Maximum	1060	1050
Average	1045	1040
St.Deviation	8	7.4

in unit square models are measured and given in Table 3.3 and Table 3.4, respectively. Again, average values of Provider 1 is better with lower standard deviations. Yet, average values of the dimensions of unit square are worse than those of single models. Besides, standard deviation of these dimensions are higher in unit square model. Since the dimensions of the model produced by Provider 1 are closer to ideal ones, Provider 1 is selected for production of the optimized 2D model, shown in Figure 2.28.

Table 3.3. t_2 Dimensions of the First 1D Optimized Models in the Square Unit Cell (in μm).

	Provider 1		Provider 2	
	490	460	460	500
	500	460	460	480
	500	460	460	410
	500	480	490	410
	510	480	500	510
	490	490	480	490
	500	470	460	420
	500	500	490	420
	490	470	500	500
	480	480	490	490
	490	470	480	440
	490	460	450	420
	460	490	500	480
	460	460	470	480
	460	460	460	470
	460	480	460	460
	470	500	500	480
	470	500	460	480
	470	500	470	460
	470	490	470	450
	480	490	500	470
	470	460	500	470
	470	500	460	470
	460	460	440	440
Minimum	460		410	
Maximum	510		510	
Average	479.4		469	
St.Deviation	15.9		25.5	

Table 3.4. t_2 Dimensions of the 1D Complementary Optimized Models in the Square Unit Cell (in μm).

	Provider 1		Provider 2	
	1050	1050	1000	1140
	1040	1030	1000	1260
	1050	1060	1070	1060
	1060	1050	1030	1050
	1050	1050	1060	1070
	1040	1040	980	1070
	1050	1040	1060	1020
	1040	1050	1030	1020
	1060	1050	1040	1010
	1040	1050	1020	1000
	1050	1040	1030	1000
	1050	1040	1020	1010
Minimum	1030		980	
Maximum	1060		1260	
Average	1047.1		1043.8	
St.Deviation	7.5		57.4	

3.2.2. Impact Test

In order to find the frequency response and band gap of the unit square produced by Provider 1, impact test is conducted via an impact hammer. The structure is suspended from its mid point, hit by the hammer from a corner and output is measured via a laser vibrometer from the opposite corner, as shown in Figure 3.9. The setup is given in Figure 3.10.

The test is performed in the direction of the two diagonals of the square, 1-4 and 2-3, and the frequency response along these paths are compared with the one obtained from FEA. As shown in Figure 3.11, the band gap obtained from FEA is

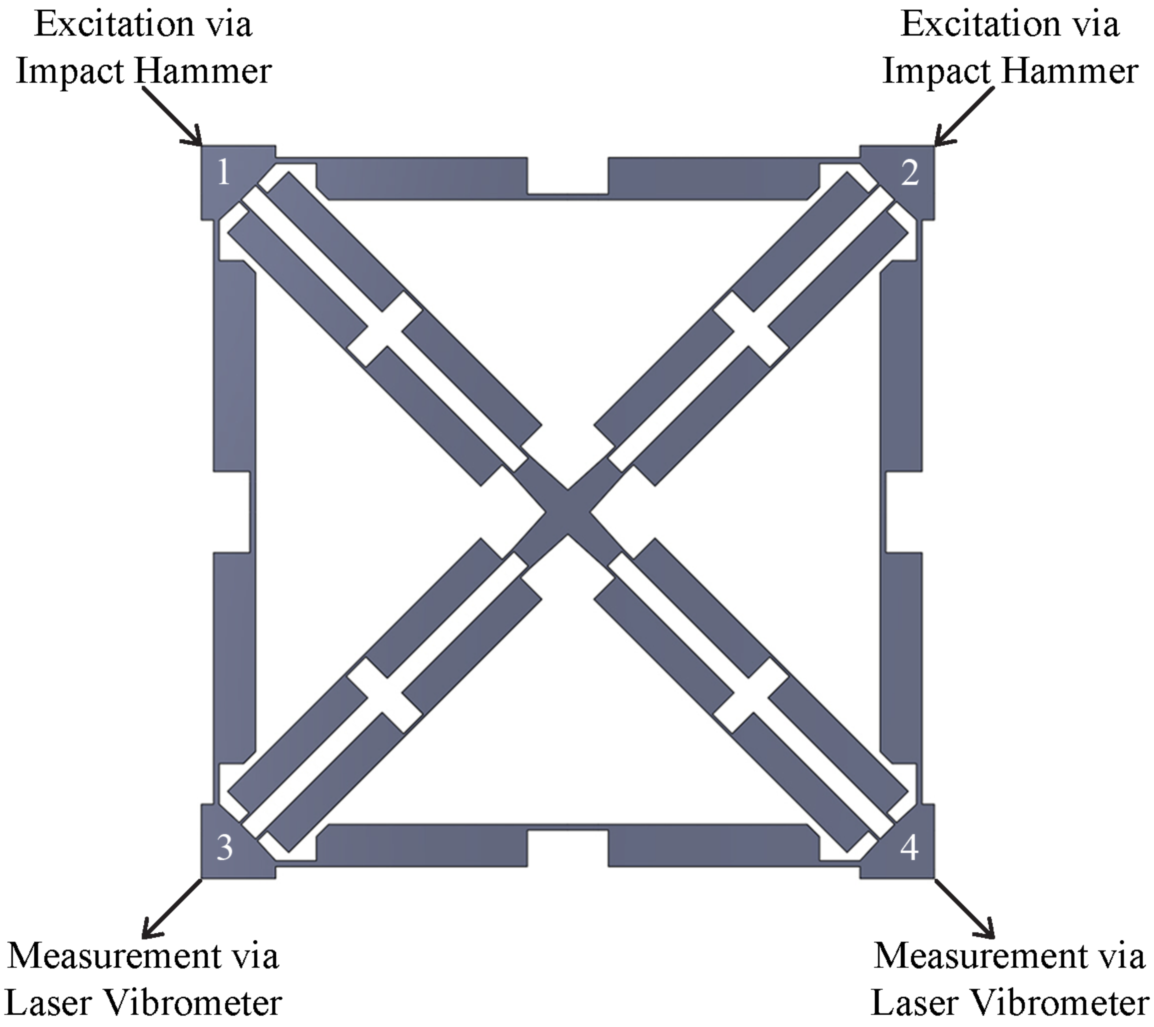

Figure 3.9. Impact Test.

deeper and narrower than that of the measurement result. These differences stem from the variations in the dimensions. Besides, experimental response has some small peaks in band gap region. These peaks correspond to the out of plane modes of the structure, which are not present in FEA, since the structure is modeled as two dimensional.

3.2.3. Frequency Response Function Estimation

There are several ways to estimate the frequency response function of the system [32]. Two of them are used in the interface of the data acquisition system used in this experiment. One is H_1 estimation, which assumes that there is no noise in the input

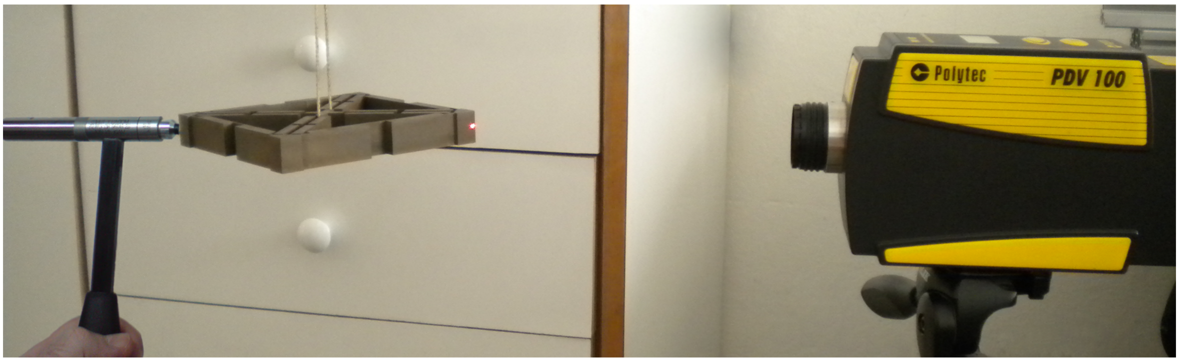

Figure 3.10. Impact Test Setup.

channel, and the other one is H_2 estimation which assumes that there is no noise in the output channel [32, 33]. In our experiments, H_1 estimation is used.

3.2.4. Shaker Test

The 2D optimized model, given in Figure 2.28, is produced by the provider 1, and given in Figure 3.12. Maximum, minimum, average and standard deviation values of t_2 sections of this structure is given in Table 3.5.

Table 3.5. Minimum, Maximum, Average and Standard Deviation Values for t_2 Dimensions of the 1D Optimized Models in the Produced 2D Model. (in μm).

	First Optimized 1D Model	Complementary Optimized 1D Model
Min	460	1020
Max	540	1100
Average	497	1047.9
St. Deviation	18.8	13.7

The structure is hung on a rigid frame, and random input is given by a shaker from the middle of one of its short edges, and the output is measured by an accelerometer from the middle of its other short edge, as shown in Figure 3.13. The average of 90 measurements is calculated in order to reduce the effect of noise in the system.

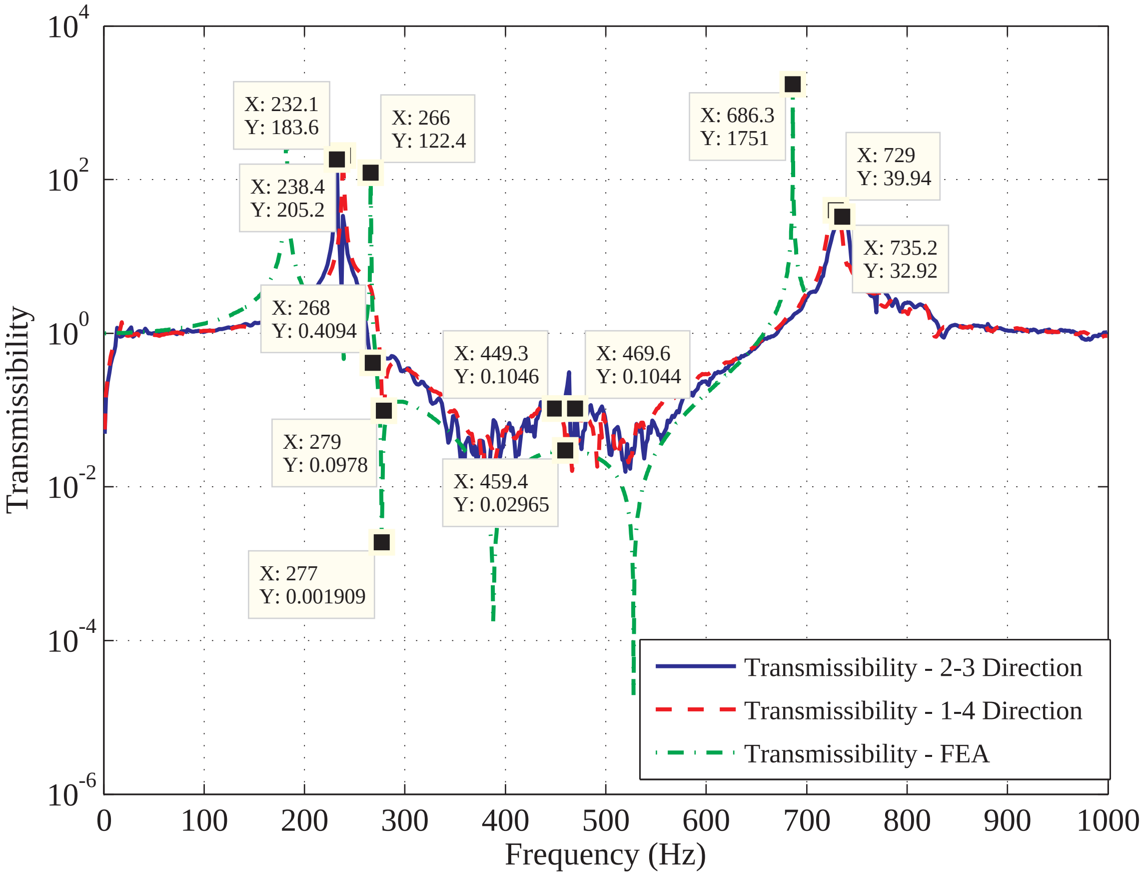

Figure 3.11. Transmissibility of the Unit Square.

Moreover, Hanning window is used to reduce the spectral leakage. The frequency response function of the structure is found by using H_1 estimation, and given in Figure 3.14. By comparing this figure with Figure 3.4, one can see that the difference between the width of the band gap is about 8%. In Figure 3.14, there is a small local peak at 442 Hz, which does not cause much harm to the band gap. However, it should not be there according to the 2D FEM analysis given in Figure 3.4. In Figure 3.15, the frequency response in the out-of-plane direction is also given. In this figure, there is also a peak at 442 Hz. Hence, the small peak at 442 Hz in Figure 3.14 is due to small amount of eccentricity in excitation. The same experiment is conducted on the same model with a PVC layer placed on top of it, which is put in order to increase the damping of the system, and frequency responses in in-plane and out-of-plane directions are given in Figure 3.16, and Figure 3.17, respectively. In Figure 3.16, the resonance peaks are smaller, which is good in terms of minimizing vibration transmission around these frequencies. However, the antiresonance notch around 300 Hz is not as deep as the one in Figure 3.14. Nevertheless, the average depth and width of the band gap is similar in these figures.

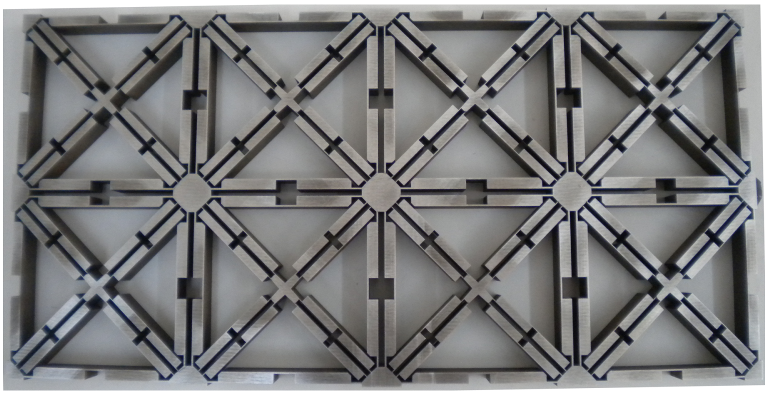

Figure 3.12. Optimized 2D Model Produced by Provider 1.

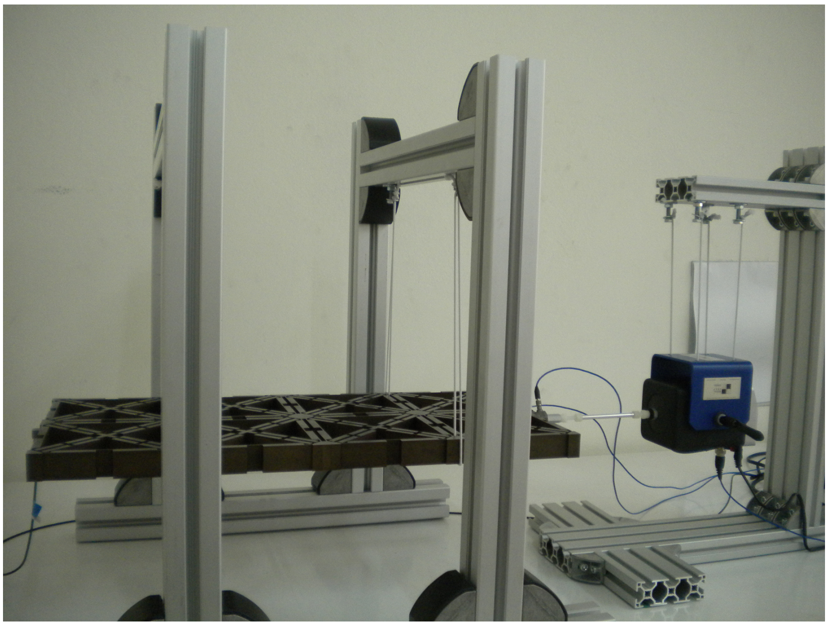

Figure 3.13. Shaker Test Setup.

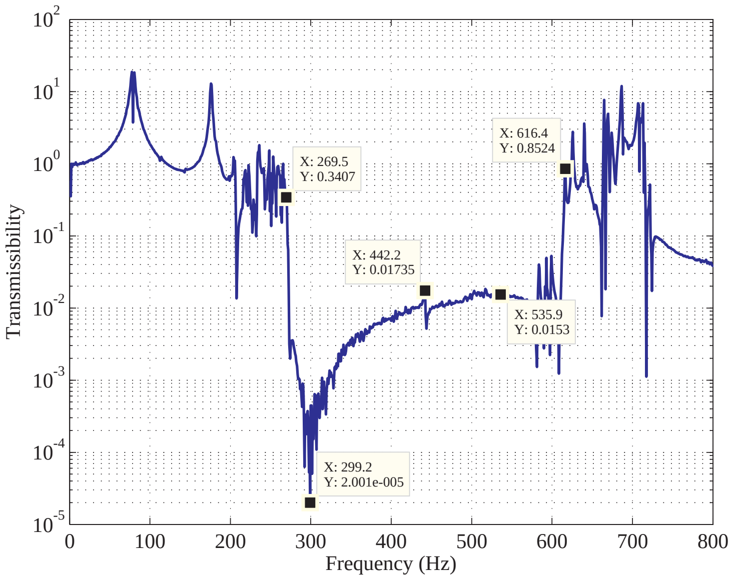

Figure 3.14. Frequency Response of the Produced 2D Model. Only 1.7% of the Input Vibration is Transmitted to the Output End in the Frequency Range 273 Hz - 583 Hz.

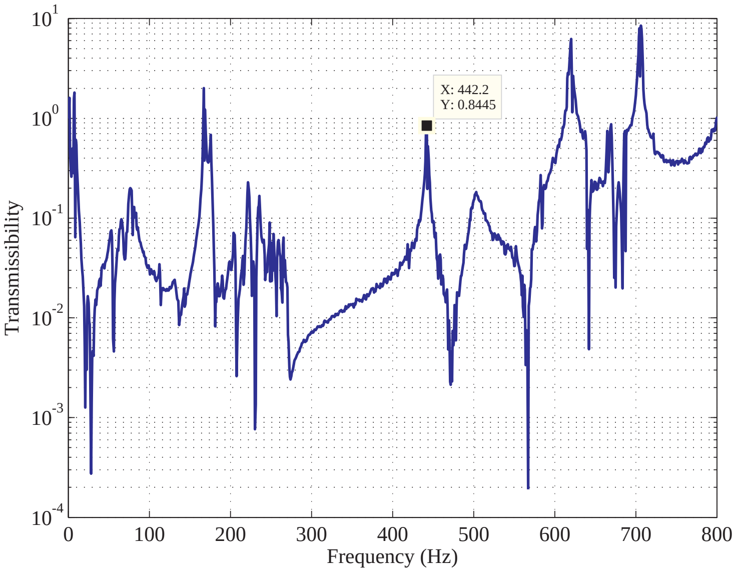

Figure 3.15. Frequency Response of the Produced 2D Model in Out-of-Plane Direction.

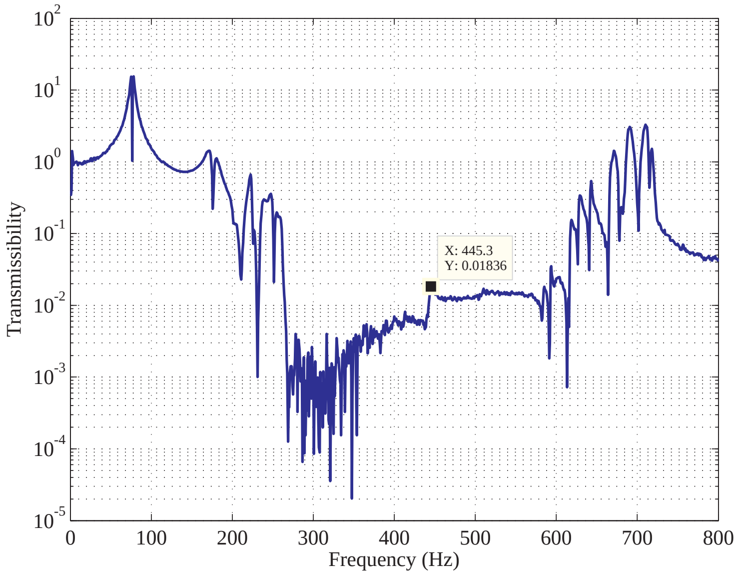

Figure 3.16. Frequency Response of the Produced 2D Model with Extra Damping. Only 1.8% of the Input Vibration is Transmitted to the Output End in the Frequency Range 263 Hz - 593 Hz.

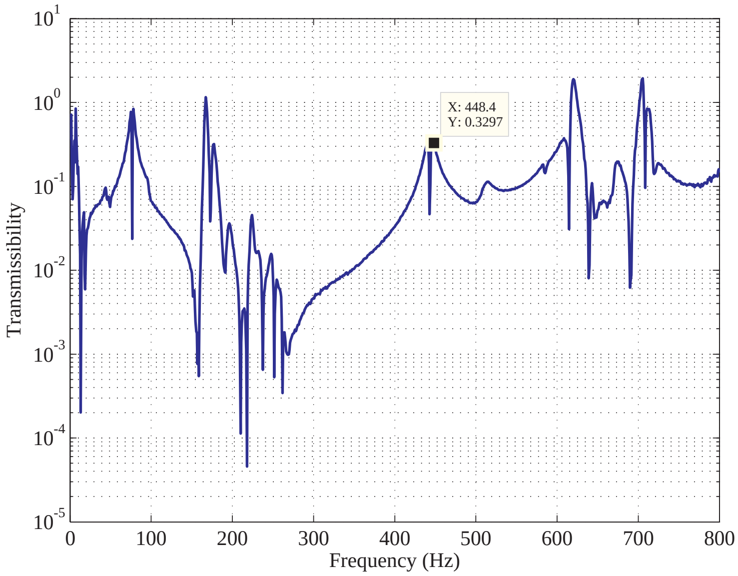

Figure 3.17. Frequency Response of the Produced 2D Model with Extra Damping in Out-of-Plane Direction.

4. CONCLUSIONS

In this thesis, a 2D periodic structure, equipped with inertial amplification mechanisms, is designed. The structure has a band gap in 300-600 Hz range.

Types of band gaps, and band gap generation methods in literature are investigated. An alternative method, inertial amplification, is proposed and examples of inertial amplification mechanisms are given. Then, a bridge-type mechanism is selected. Equation of motion of this mechanism is found by Lagrange's method, and the resonance and the antiresonance frequencies are calculated.

A 1D distributed parameter model, equivalent to the inertial amplification mechanism selected, is designed. The equivalent mass and stiffness values are found using energy methods. The first resonance and antiresonance frequencies are calculated by using these equivalent mass and stiffness values. Then, the second natural frequency of the distributed parameter model is also found by using Lagrange's method. The band gap is expected to be in between the first and second natural frequencies.

Finite Element Method is also used in order to find the natural frequencies and the frequency responses of the 1D distributed parameter model. When compared with the FEA results, the error in analytical calculations is about 2.5%. Since it is more accurate, Finite Element Method is used in optimization study.

The 2D model is designed as an assembly of two different 1D unit models. First, a 1D model is optimized so that the ratio of first natural frequency to the second natural frequency is minimized. The model is planned to be produced with wire EDM method, so the thickness of the thinnest sections are set to 0.5 mm, since it is considered as the minimum thickness for a good tolerance with the selected production technique. After the first 1D model is optimized, the second 1D model is optimized. The optimization criterion is set as the minimization of the sum of the differences between the first and the second natural frequencies of the two 1D models.

After the two 1D models are optimized, the 2D model is constructed and it is subjected to Finite Element Analysis using ABAQUS. The band gap is generated in 272-607 Hz range. During production phases, some deviations might occur in dimensions. In order to take them into account, three models with different amount of standard deviations are subjected to FEA. Besides, the effect of damping on the frequency response is also found by analyzing the model for three different damping values.

The 2D optimized model is produced and subjected to random vibrations using a shaker. Vibration output of the model is measured from the opposite edge by an accelerometer. The band gap is generated in 273-583 Hz range, which is consistent with the FEA results.

REFERENCES

1. Martinsson, P. G. and A. B. Movchan, “Vibrations of Lattice Structures and Phononic Band Gaps”, *The Quarterly Journal of Mechanics and Applied Mathematics*, Vol. 56, No. 1, pp. 45–64, 2003.

2. Jensen, J. S., “Phononic Band Gaps and Vibrations in One- and Two-dimensional Mass-spring Structures”, *Journal of Sound and Vibration*, Vol. 266, No. 5, pp. 1053–1078, 2003.

3. Soliman, Y. M., M. F. Su, Z. C. Leseman, C. M. Reinke, I. El-Kady and R. H. Olsson, “Phononic Crystals Operating in the Gigahertz Range with Extremely Wide Band Gaps”, *Applied Physics Letters*, Vol. 97, No. 19, p. 193502, 2010.

4. Norris, R., P. Nieva and J. Hamel, “Analytical Analysis of a Discrete MEMS Diatomic Mass-spring Phononic Band Gap Crystal for Vibration Stabilization Applications”, *Sensors*, pp. 506–509, IEEE, 2008.

5. Mohammadi, S., A. A. Eftekhar, A. Khelif, W. D. Hunt and A. Adibi, “Evidence of Large High Frequency Complete Phononic Band Gaps in Silicon Phononic Crystal Plates”, *Applied Physics Letters*, Vol. 92, No. 22, p. 221905, 2008.

6. Yablonovitch, E., “Photonic Band-gap Structures”, *Journal of the Optical Society of America B*, Vol. 10, No. 2, pp. 283–295, 1993.

7. Sigalas, M. and E. N. Economou, “Band Structure of Elastic Waves in Two Dimensional Systems”, *Solid State Communications*, Vol. 86, No. 3, pp. 141–143, 1993.

8. Jensen, J. S., O. Sigmund, J. J. Thomsen and M. P. Bendsoe, “Design of Multiphase Structures with Optimized Vibrational and Wave-transmitting Properties”, *15th Nordic Seminar on Computational Mechanics*, pp. 63–66, 2002.

9. Phani, A. S., J. Woodhouse and N. A. Fleck, “Wave Propagation in Two-dimensional Periodic Lattices”, *The Journal of the Acoustical Society of America*, Vol. 119, No. 4, pp. 1995–2005, 2006.

10. Wen, J., D. Yu, G. Wang and X. Wen, “Directional Propagation Characteristics of Flexural Wave in Two-dimensional Periodic Grid-like Structures”, *Journal of Physics D: Applied Physics*, Vol. 41, p. 135505, 2008.

11. Liu, Z., C. T. Chan and P. Sheng, “Three-component Elastic Wave Band-gap Material”, *Physical Review B*, Vol. 65, No. 16, p. 165116, 2002.

12. Liu, Y. H., C. C. Chang, R. L. Chern and C. C. Chang, “Phononic Band Gaps of Elastic Periodic Structures: A Homogenization Theory Study”, *Physical Review B*, Vol. 75, No. 5, p. 054104, 2007.

13. Watanabe, Y. and N. Sugimoto, “Flexural Wave Propagation in a Spatially Periodic Structure of Articulated Beams”, *Wave Motion*, Vol. 42, No. 2, pp. 155–167, 2005.

14. Parmley, S., T. Zobrist, T. Clough, A. Perez-Miller, M. Makela and R. Yu, “Phononic Band Structure in a Mass Chain”, *Applied Physics Letters*, Vol. 67, p. 777, 1995.

15. Platts, S. B., N. V. Movchan, R. C. McPhedran and A. B. Movchan, “Transmission and Polarization of Elastic Waves in Irregular Structures”, *Journal of Engineering Materials and Technology*, Vol. 125, p. 2, 2003.

16. Herzenberg, A., K. L. Kwok and F. Mandl, “Resonance Scattering Theory”, *Proceedings of the Physical Society*, Vol. 84, p. 477, 1964.

17. Widmer, D. S., *Phononic Quasicrystals*, Ph.D. Thesis, ETH ZÜRICH, 2007.

18. Talmant, M., G. Quentin, J. L. Rousselot, J. V. Subrahmanyam and H. Überall,

"Acoustic Resonances of Thin Cylindrical Shells and the Resonance Scattering Theory", *The Journal of the Acoustical Society of America*, Vol. 84, p. 681, 1988.

19. Wehling, T. O., S. Yuan, A. I. Lichtenstein, A. K. Geim and M. I. Katsnelson, "Resonant Scattering by Realistic Impurities in Graphene", *Physical Review Letters*, Vol. 105, No. 5, p. 56802, 2010.

20. Yilmaz, C. and G. M. Hulbert, "Theory of Phononic Gaps Induced by Inertial Amplification in Finite Structures", *Physics Letters A*, Vol. 374, No. 34, pp. 3576–3584, 2010.

21. Yilmaz, C., G. M. Hulbert and N. Kikuchi, "Phononic Band Gaps Induced by Inertial Amplification in Periodic Media", *Physical Review B*, Vol. 76, No. 5, p. 054309, 2007.

22. Yoon, H. S., G. Washington, P. Eyabi, M. Radhamohan, S. W. Woodard and R. Dayton, "A Millimeter-stroke Piezoelectric Hybrid Actuator Using Hydraulic Displacement Amplification Mechanism", *2006 IEEE International Symposium on Industrial Electronics*, Vol. 4, pp. 2809–2813, IEEE, 2006.

23. Ninomiya, T., Y. Okayama, Y. Matsumoto, X. Arouette, K. Osawa and N. Miki, "MEMS-based Hydraulic Displacement Amplification Mechanism with Completely Encapsulated Liquid", *Sensors and Actuators A: Physical*, Vol. 166, No. 2, pp. 277–282, 2011.

24. Yilmaz, C. and N. Kikuchi, "Analysis and Design of Passive Low-pass Filter-type Vibration Isolators considering Stiffness and Mass Limitations", *Journal of Sound and Vibration*, Vol. 293, No. 1, pp. 171–195, 2006.

25. Uchikawa, T., "Mechanical Amplification Mechanism Combined with Piezoelectric Elements", US Patent 4,570,095, 1986.

26. Sano, M., "Displacement Amplification Mechanism Using Piezoelectric Element",

US Patent 5,191,252, 1993.

27. Berton, S. and J. E. Bolander, “Amplification System for Supplemental Damping Devices in Seismic Applications”, *Journal of Structural Engineering*, Vol. 131, p. 979, 2005.

28. Rivin, E., *Passive Vibration Isolation*, ASME Press, New York, 2003.

29. Ma, H. W., S. M. Yao, L. Q. Wang and Z. Zhong, “Analysis of the Displacement Amplification Ratio of Bridge-type Flexure Hinge”, *Sensors and Actuators A: Physical*, Vol. 132, No. 2, pp. 730–736, 2006.

30. Lobontiu, N. and E. Garcia, “Analytical Model of Displacement Amplification and Stiffness Optimization for a Class of Flexure-based Compliant Mechanisms”, *Computers & Structures*, Vol. 81, No. 32, pp. 2797–2810, 2003.

31. Brillouin, L., *Wave Propagation in Periodic Structures*, Dover, New York, 1953.

32. McConnell, K., *Vibration Testing*, Wiley, New York, 1995.

33. Ewins, D., *Modal Testing*, Wiley, Philadelphia, 2001.